Polymorphism and melt in high-pressure tantalum. II. Orthorhombic phases

Justin B. Haskins and John A. Moriarty

Phys. Rev. B **98**, 144107 — Published 11 October 2018

DOI: 10.1103/PhysRevB.98.144107

Polymorphism and Melt in High-Pressure Tantalum II. Orthorhombic Phases

Justin B. Haskins[1] and John A. Moriarty[2]

[1]AMA, Inc., NASA Ames Research Center, Moffett Field, California 94035 USA

[2]Lawrence Livermore National Laboratory, Livermore, California 94551-0808 USA

Abstract

Continuing uncertainty in the high-pressure melt curves of bcc transition metals has spawned renewed research interest in the phase diagrams of these materials, with tantalum becoming an important prototype. The present paper extends the quantum-based investigation of high-T,P polymorphism and melt in Ta that was begun in Paper I [Phys. Rev. B **86**, 224104 (2012)] on five candidate cubic and hexagonal structures (bcc, A15, fcc, hcp and hex-ω) to here treat four promising orthorhombic structures (*Pnma*, *Fddd*, *Pmma* and α-U). Using DFT-based MGPT multi-ion potentials that allow accurate MD simulations of large systems, we showed in Paper I that the mechanically unstable fcc, hcp and hex-ω structures can only be stabilized at high-T,P by large anharmonic vibrational effects, requiring systems of ~ 500 atoms to produce size-independent melt curves and reliable calculations of thermodynamic stability. This reversed a previous small-cell quantum-simulation prediction of a high-T,P hex-ω phase. Subsequent DFT calculations have now suggested a more energetically favorable and mechanically stable *Pnma* structure, which again small-cell quantum simulations predict could be a high-T,P phase. Our present MGPT total-energy and phonon calculations show that not only *Pnma*, but all four orthorhombic structures considered here, are similarly energetically favorable, and that *Fddd* in addition to *Pnma* is mechanically stable up to 420 GPa. MGPT-MD simulations further reveal spontaneous temperature-induced *Pnma* → bcc and *Fddd* → bcc transformations at modest temperatures, peaking at ~ 1450 K near 100 GPa. At high temperatures near melt, we find T-dependent c/a and b/a axial ratios and large stabilizing anharmonicity present in all four orthorhombic structures. The

anharmonicity drives significantly larger melt size effects, requiring systems of ~ 1000–4000 atoms to produce converged melt curves for reliable predictions of relative thermodynamic stability. In the large-cell limit, with ~ 40,000 solid-phase atoms and accurate two-phase MGPT-MD melt simulation, we find that *Pnma*, *Fddd* and α-U have melt temperatures that are equal to bcc over small pressure ranges in the vicinity of 100 GPa, but that the orthorhombic melt temperatures never exceed bcc up to 420 GPa. This finding suggests that *Pnma*, *Fddd* and α-U remain highly competitive metastable phases that could co-exist with bcc and possibly be observed experimentally. Finally, to add additional insight into our results we have constructed global Helmholtz free energies for the A15, *Pnma* and *Fddd* phases of Ta, complementing previous free energies obtained for the bcc, fcc, and liquid phases.

I. INTRODUCTION

The long-standing controversy in bcc transition metals between "flat" static melt curves obtained from early laser-heated diamond-anvil-cell (DAC) measurements [1-3] and "steep" dynamic melt curves inferred from dynamic isobaric [4-7] and shock [8-11] measurements has renewed research interest in the high-temperature (T), high-pressure (P) phase diagrams of these materials, with tantalum (Ta) emerging as an important specific example that has attracted considerable recent attention [12-21]. In 2010, Burakovsky *et al.* [12] used small-cell (< 150 atoms) quantum molecular dynamics (QMD) melt simulations, based on first-principles density functional theory (DFT) [22] and Z-melt methodology [23], to predict a hexagonal omega (hex-ω) phase in Ta at high temperature above 70 GPa. Shortly thereafter, in Paper I of this series [13], we examined possible high-T,P polymorphism in five cubic and hexagonal phases of Ta with complementary DFT-based MGPT (model generalized pseudopotential theory) multi-ion interatomic potentials [13,14], which allow accurate treatment of much larger system sizes in MGPT-MD simulations. We found significant melt size effects for all non-bcc phases studied, requiring a minimum of ~ 500 atoms in the solid to simulate a reliable bulk melt curve for these phases. While in the small-cell limit we confirmed the QMD, Z-melt hex-ω prediction, we found that in the large-cell limit, with accurate two-phase MGPT-MD simulations and ~ 40,000 atoms in the solid, that bcc produces the highest melt temperatures at all pressures to 420 GPa and hence is thermodynamically the most stable of the phases considered.

We also showed in Paper I that the corresponding high-T mechanical stability of hex-ω is unexpectedly complex, with a bifurcation in its mechanical behavior as a function of c/a ratio that impacts the metastability of this structure. Both DFT and MGPT quasi-harmonic phonon calculations show that at $T = 0$ the hex-ω structure has imaginary phonon frequencies at pressures up to at least 420 GPa, and hence is mechanically unstable at low temperature for all pressures of interest. At high temperature, however, large anharmonic vibrational effects occur that can aid in producing mechanical stability and hence bulk metastability. For low values of $c/a < 0.54$, such metastability is indeed realized in MGPT-MD simulations, although at a large free-energy cost that keeps the

hex-ω melt curve far below that of bcc. For larger, and more normal, values of $c/a > 0.54$, on the other hand, the high-T mechanical stability, as measured in MD simulations by the calculated stress tensor, is poor and a partial transformation to bcc occurs. The transformation to bcc is incomplete because of the hex-ω boundary conditions imposed by the MD simulations, so the physical inference is that the hex-ω structure remains mechanically unstable in the high-T, $c/a > 0.54$ regime. This conclusion is now supported by the recent DFT self-consistent phonon calculations of Yao and Klug [15] and of Liu *et al*. [16]. Such calculations impart a T-dependence to the phonon frequencies and thereby capture at least part of the anharmonic vibrational effects at high temperature. These authors find that imaginary phonon frequencies, and hence mechanical instability, persist in the hex-ω structure at high-T,P conditions up to 400 GPa and 6000 K, and up to 300 GPa and 7000 K, respectively.

At the same time, there have been continuing experimental indications [17,18] of a possible bcc to hex-ω phase transition in strongly shocked Ta and Ta-W alloys. Previously, Hsiung and Lassila [24] had found evidence of hex-ω in recovered Ta and Ta-W samples that had been shocked to 145 GPa. In more recent shock experiments at only 30 GPa, however, Hsiung [17] found that hex-ω was absent in recovered Ta and Ta-5%W samples, and was only present in a Ta-10%W alloy. In new laser-driven shock experiments on Ta at 70 GPa, Lu *et al.* [18] have reported both *in situ* and sample recovery evidence for hex-ω, suggesting a threshold shock pressure in the range 30-70 GPa for this phenomenon to occur in the elemental material. In any case, a clear quantum-based explanation for the phenomenon is still lacking, and in light of the above discussion, any such explanation must at the very least be *environmentally dependent* and involve dynamic nonequilibrium and other factors well removed from the equilibrium phase diagram itself for pure Ta.

Consequently, current theoretical research attention on the equilibrium phase diagram in Ta has now turned away from cubic and hexagonal structures, such as hex-ω, and towards the possibility of lower-energy orthorhombic phases occurring at high-T,P conditions. This interest follows recent DFT [15,16] and small-cell QMD [19]

indications of a possible high-*T*,*P* *Pnma* phase in Ta. In contrast to hex-ω, DFT quasi-harmonic phonon calculations by Yao and Klug [15] and Liu *et al.* [16] on *Pnma* have produced all real phonon frequencies to 400 GPa and 250 GPa, respectively, and hence low-temperature mechanical stability at the pressures of interest. Using small-cell (64 atom) DFT-based metadynamics simulations, Yao and Klug further studied a possible high-*T*,*P* bcc to *Pnma* phase transition, and elaborated a plausible Burgers-like transition path between the two structures. Subsequently, Burakovsky *et al.* [19] used ~ 500-atom QMD, Z-melt simulations on *Pnma* Ta to predict a bcc to *Pnma* transition at high temperature above 200 GPa.

In the present work, we have now extended our MGPT Ta polymorphism studies reported in Paper I to four promising candidate orthorhombic structures: *Pnma*, *Fddd*, *Pmma* and *Cmcm*. All of these structures are either observed phases in heavy metals or have been predicted to be competitive phases in bcc transition metals. As a whole, we find these orthorhombic phases to be highly competitive with bcc in Ta at high-*T*,*P* conditions, with each structure exhibiting good to excellent mechanical stability in this regime. But at the same time, these structures exhibit very large anharmonic effects at high temperature that drive significantly larger melt size effects than we found in the cubic and hexagonal structures. These size effects, which now range up to ~ 1000–4000 atoms, depending on the melt method and simulation cell shape, again can significantly alter phase predictions, calling into question the above DFT and QMD predictions on *Pnma*.

In Fig. 1 we update our baseline starting point with the best current experimental and theoretical knowledge about high-pressure bcc melting in Ta. In particular, there have been two improved laser-heated DAC measurements of bcc melting [20,21] that yield significantly higher melt temperatures as a function of pressure than in the earlier experiments [1,2]. In the new experiments, both Dewaele *et al.* [20] and Karandikar and Boehler [21] have identified and addressed the important issues of chemical contamination in the DAC and resulting chemical reactions with the Ta sample. These workers differ, however, in their approaches to the melt-temperature measurement itself, with Dewaele *et al.* finding higher melt temperatures, but with large error bars. The new DAC melt data are compared with the best available DFT-based bcc melt curves and with

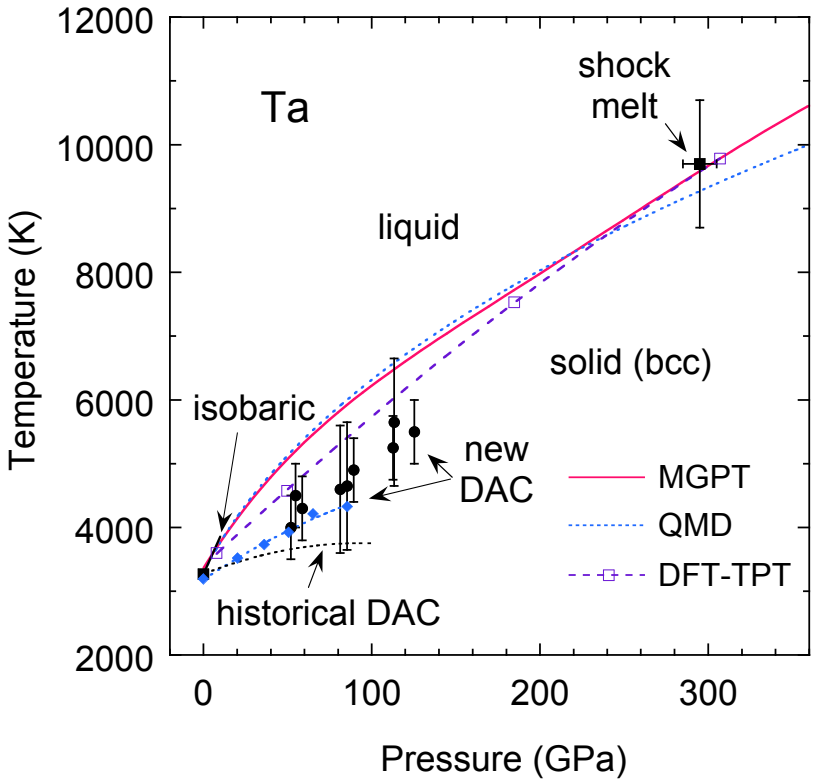

FIG. 1. High-pressure bcc melting in Ta, as obtained from MGPT free energies [14], QMD simulations [12], and DFT-TPT calculations [25], and compared with experimental data from both historical [1,2] and new [20,21] DAC measurements (solid circles with error bars [20] and solid diamonds [21]), and with data from isobaric [5] and shock [8,11] measurements.

previous static and dynamic data for Ta. The three theoretical melt curves displayed in Fig. 1 derive from the accurate MGPT free energies of Moriarty and Haskins [14], from the QMD, Z-melt simulations of Burakovsky *et al.* [12], and from the DFT-based thermodynamic-perturbation-theory (TPT) calculations of Taioli *et al.* [25]. The MGPT and QMD melt curves closely agree with each other up to pressures of ~ 250 GPa, as well as with the initial low-pressure melting slope obtained from isobaric expansion data [5]. The MGPT and DFT-TPT melt curves agree well with each other above ~ 180 GPa and with the shock melting point near 300 GPa [8,11]. In the DAC pressure regime below about 135 GPa, the DFT-TPT melt curve is closest to the new DAC data and within the

error bars of the Dewaele *et al.* results [20]. In all of the DAC measurements to date no other solid phase than bcc has ever been reported.

The outline of the present paper is as follows. In Sec. II we briefly review our theoretical and computational methods, with special attention given to the complicating features that the more complex orthorhombic structures present to MGPT-MD melt simulations. In all MGPT calculations considered here we use the same high-quality Ta6.8*x* multi-ion potentials employed in Paper I and in Ref. [14]. We find, however, that the simplified Z-melt method, while useful for comparisons and providing lower bounds on melt size effects, does not produce reliable converged melt curves for any of the orthorhombic structures considered. Consequently, most of our present melt simulations are carried out with the more accurate two-phase method previously discussed in Paper I. In Sec. III we consider the low-temperature structural and mechanical stability of our four candidate orthorhombic structures, including the interesting possibility of spontaneous temperature-induced transitions to bcc for the *Pnma* and *Fddd* phases. In Sec. IV we then address high-temperature mechanical stability and melt in the same candidate structures, including large anharmonic energies and melt size effects, and the calculation of accurate large-cell two-phase melt curves for comparison with bcc in each case. In Sec. V we calculate additional global free energies for the A15, *Pnma* and *Fddd* phases, complementing previous free energies obtained in Paper I for the bcc, fcc and liquid phases, and providing additional insight into our results. Finally, in Sec. VI we summarize all of our Ta polymorphism results to date and draw conclusions.

II. THEORETICAL and COMPUTATIONAL METHODS

In this section we briefly review relevant aspects of our theoretical and computational methods used in the remainder of this paper, including the origin and application of MGPT interatomic potentials, the two-phase melt method and its application to complex orthorhombic structures, and the calculation of global free energies.

A. MGPT interatomic potentials

Within DFT quantum mechanics, generalized pseudopotential theory (GPT) provides a first-principles approach to quantum-based interatomic potentials in transition metals [26]. The simplified *model* GPT or MGPT [27] used here is derived from the GPT through a series of systematic approximations applicable to mid-period transition metals with nearly half-filled *d* bands, and permits efficient large-scale atomistic simulations with full quantum mechanical realism, including the inherently long-ranged nature of the interatomic interactions. In both the GPT and MGPT applied to a bulk transition metal at atomic volume Ω, the real-space total-energy functional takes the form

$$E_{\rm tot}(\mathbf{R};\Omega) = NE_{\rm vol}(\Omega) + \frac{1}{2}{\sum_{i,j}}' v_2(ij;\Omega) + \frac{1}{6}{\sum_{i,j,k}}' v_3(ijk;\Omega) + \frac{1}{24}{\sum_{i,j,k,l}}' v_4(ijkl;\Omega) \ , \qquad (1)$$

where $\mathbf{R} \equiv \{\mathbf{R}_i\}$ denotes the variable N ion positions in the metal, and the prime on each summation sign denotes the exclusion of all self-interaction terms from the summation. The leading volume term in Eq. (1), $E_{\rm vol}$, as well as the two-ion radial-force pair potential v_2, and the three- and four-ion angular-force potentials, v_3 and v_4, depend explicitly on the atomic volume Ω, but are structure independent and transferable to all bulk ion configurations, either ordered or disordered. The specific refined Ta6.8*x* MGPT potentials used in both Paper I and in the present paper are most completely described in Ref. [14]. Extensive tests of the Ta6.8x potentials for cubic and hexagonal structures as well as the liquid are discussed in Ref. [14], as well as in Paper I. Additional tests on the present orthorhombic structures are discussed in Sec. III.

As in Paper I, we apply the Ta6.8*x* potentials in all calculations using the efficient matrix representation of MGPT [28], as implemented in the parallel molecular dynamics code *ddcMD* [29] and in the open-source MD code LAMMPS [30]. The Ta6.8*x* potentials themselves are available as part of the USER-MGPT package included in LAMMPS. The advanced MGPT capability of temperature-dependent potentials [31], which allows direct treatment of electron temperature in MD simulations, is not believed to be important for wide-band 5*d* metals like Ta and has *not* been used in constructing the present Ta6.8*x* potentials, which neglect electron-thermal effects entirely. In this regard, electron-thermal contributions have been shown to affect the bcc melt curve in Ta by less than 5% [14,32]. The small neglected electron-thermal contributions in Ta can be included after the fact, if desired, in the global free energy of a given phase, as described below in Sec. IIC.

B. Two-phase and Z-method melt simulations for orthorhombic structures

Our primary dynamic two-phase melt method [13,31], as applied in the *ddcMD* code, is a refined and robust version of the solid-liquid coexistence method of Morris *et al*. [33]. As in other modern and equivalent coexistence melt methods (*e.g.*, Hernandez *et al.* [34]), our approach replaces constant-volume coexistence in the Morris *et al.* method with the desired thermodynamic condition of constant-pressure coexistence. In normal melting metals like Ta, of course, there is an increase in volume upon melting that is not accounted for in the Morris *et al.* method, but is correctly treated in our constant-pressure two-phase method. In our approach, equilibrated solid and liquid subcells of equal size and shape, and maintained at equal constant pressure, are placed in contact, and the movement of the solid-liquid interface is monitored with a sensitive order parameter as a function of pressure for a trial melt temperature T_{m}. The equilibrium melting pressure $P_{\mathrm{m}}(T_{\mathrm{m}})$ is achieved when the solid-liquid interface remains stationary and neither the solid nor the liquid phase is growing at the expense of the other. Additional technical details on our two-phase melt method are given in Paper I. The method has been extensively tested and successfully applied to complex *d*- and *f*-electron metals described by quantum-mechanical forces, including Ta [13,14], Mo [31] and U [35,36].

Also in this regard, it is well known that the accuracy of two-phase melt methods increases with cell size, and that significant cell sizes are needed to apply the method reliably. Indeed, Morris *et al.* already discussed these issues in their original paper [33]. Even to melt weakly anharmonic fcc Al with short-range empirical forces, Morris *et al.* found it necessary to use a shape-corrected solid subcell of at least 512 atoms, and considered subcells as large as 32,768 atoms. Today the use of large cell sizes in two-phase melting simulations for metals is really quite common [13,14,34,37,38] whether or not strong anharmonic effects are present. As in Paper I, we consider here solid-phase cells as large as $\sim 40{,}000$ atoms.

The two-phase Ta melt curves treated in Paper I involved only cubic and hexagonal structures, whose lattice vectors and MD subcells are explicitly dependent on the volume Ω, and for the hexagonal structures on an additional c/a ratio. The present orthorhombic structures and MD subcells, however, depend on three parameters: Ω plus c/a and b/a axial ratios. In addition, the c/a and b/a ratios are significantly temperature dependent and cannot be determined from Ω alone. The temperature-dependent nature of the orthorhombic structures thus presents a challenge to the determination of the melt curve, as the correct melt temperature would need to be known *a priori* before melt assessment. We, therefore, have adopted an iterative approach to melt determination. Starting guesses for the structure and subcell shape are evaluated at a corresponding bcc melt volume Ω_m using an optimization procedure discussed in Sec. IV. After determining the melt temperature T_{m} at this volume, the shape of the subcell is optimized at these conditions, and a new melt curve is determined from the corrected structure. This procedure can be iterated until convergence, though we have found in practice that a single iteration correctly predicts the melt curve to high precision.

A limited number of MGPT-MD Z-method melt calculations on the *Pnma* structure also have been carried out in this work for the purposes of examining size effects and making direct comparison with the QMD Z-melt calculations of Burakovsky *et al.* [19]. These additional Z-melt calculations have been performed with the LAMMPS code and take into account the above considerations for the c/a and b/a axial ratios, but were otherwise performed as described in Paper I. In this regard, it should also be emphasized

that our implementation of the Z-method melting is entirely *static*, unlike the more common *dynamic* versions of the Z method [12,19,23]. This is an important distinction in the present context, because our static Z method eliminates the overheating and hysteresis present in dynamic Z methods as sources of melt size effects. Thus the primary origin of melt size effects in out Z-melt simulations is the same as in our two-phase melt simulations: anharmonic vibrational effects needed to stabilize otherwise unstable solid phases at high temperature.

C. Global free energies

The basic thermodynamic functions of wide-band 5*d* transition metals like Ta are well described by the conventional weak-coupling model, in which the Helmholtz free energy $A_{\rm tot}$ can be calculated as a sum of cold $(T=0)$, ion-thermal, and electron-thermal contributions:

$$A_{\rm tot}(\Omega,T) = E_0(\Omega) + A_{\rm ion}(\Omega,T) + A_{\rm el}(\Omega,T) \ . \qquad (2)$$

The cold energy E_0 can be accurately evaluated with MGPT Ta6.8*x* potentials via Eq. (1) for all other solid structures of interest. The ion-thermal free-energy component $A_{\rm ion}$ in Eq. (2) can also be evaluated entirely from the Ta6.8*x* potentials, although this is only straightforward for solid structures that are mechanically stable at low temperature, such as bcc, where standard quasiharmonic lattice dynamics (QHLD) can be applied and $A_{\rm tot}(\Omega,T)$ can be built up from a zero-temperature starting point. In this case, $A_{\rm ion}(\Omega,T)$ can be directly obtained as a function of volume and temperature by smoothly joining QHLD free energies with efficient reversible-scaling MD (RSMD) calculation of high-temperature anharmonic free-energy contributions [14]. The final small electron-thermal free-energy component $A_{\rm el}$ in Eq. (2) embodies the remaining effects of temperature on the structure and occupation of the electronic states of the system. A useful high-temperature treatment of $A_{\rm el}(\Omega,T)$ has previously been developed for Ta from configuration-averaged, finite-temperature DFT calculations in the bcc and liquid phases, using atomic configurations obtained from MGPT-MD simulations [32]. To lowest order it was found that at high temperature

$$A_{\rm el}(\Omega,T) = -\frac{1}{2}\alpha(\Omega)T^2 \ , \tag{3}$$

where $\alpha(\Omega)$ is independent of structure. This baseline scheme was used successfully in Ref. [14] to determine very accurate free energies for the bcc phase of Ta. We use this scheme here to obtain an additional global free energy for the metastable A15 phase in Sec. V.

For the liquid and for other solid phases of Ta that are either mechanically unstable at low temperature or undergo *T*-induced phase transitions at intermediate temperatures, $A_{\rm ion}$ must first be established independently along an appropriate finite-temperature reference curve. In the liquid, this can be accomplished very accurately by making a precise thermodynamic integration from a known reference system along a chosen high-temperature isotherm. One can then use RSMD simulations to extend $A_{\rm tot}(\Omega,T)$ downward in temperature from that reference point, as described in Ref. [14]. For each remaining solid phase, one can then combine $A_{\rm ion}$ for the liquid with a simulated two-phase melt curve to obtain $A_{\rm ion}$ along the solidus melt line for that phase. One can then similarly use RSMD simulations to extend $A_{\rm tot}(\Omega,T)$ upward and downward in temperature from the reference melt line, as discussed in Ref. [14] for the metastable fcc phase. We here apply this technique to calculate global free energies for the orthorhombic *Pnma* and *Fddd* phases in Sec. V.

III. LOW-*T* STRUCTURAL and MECHANICAL STABILITY of ORTHORHOMBIC PHASES

In this section we first discuss and visualize the structural details of our four candidate orthorhombic phases: *Pnma*, *Fddd*, *Pmma*, and *Cmcm*. We then consider the relative $T = 0$ structural phase stability, as measured by relaxed total-energy calculations, and the corresponding mechanical stability, as measured by the calculated quasiharmonic phonon spectra, of each of these phases as a function of volume over the pressure range of interest up to 420 GPa. We also discuss the interesting phenomenon of *T*-induced phase transitions at moderate temperatures in the cases of *Pnma* and *Fddd*, as uncovered by MGPT-MD simulations.

A. Description of candidate structures

Orthorhombic structures are common in heavy metals. Observed orthorhombic phases also often appear in close proximity to a high-temperature bcc melting phase [39], and there usually exists an "easy" transition path between the orthorhombic structure and bcc, as elaborated for *Pnma* by Yao and Klug [15].

The *Pnma* space group is the observed high-pressure structure of Am-IV between about 17 and 100 GPa [40], and also the observed structure of Ca-VI above 158 GPa [41]. *Pnma* is a simple orthorhombic structure with four atoms per primitive cell, located on equivalent sites and defined by two internal structural parameters denoted as *x* and *z*. In terms of lattice constants *a*, *b* and *c*, the lattice vectors (**A**) and basis vectors (**b**) of *Pnma* are

$$\begin{aligned} \mathbf{A}_1 &= (a,0,0) \\ \mathbf{A}_2 &= (0,b,0) \\ \mathbf{A}_3 &= (0,0,c) \end{aligned} \qquad \begin{aligned} \mathbf{b}_1 &= (a/2-x, b/4, z-c/2) \\ \mathbf{b}_2 &= (-x, b/4, -z) \\ \mathbf{b}_3 &= (x, -b/4, z) \\ \mathbf{b}_4 &= (x-a/2, -b/4, c/2-z) \end{aligned} \quad . \tag{4}$$

Of course, as is always the case for any structure, the basis vectors may be chosen in multiple equivalent ways.

The *Fddd* space group is the observed high-temperature structure of γ-Pu near 600-700 K [39], and also the observed high-pressure structure of Am-III between about 10 and 17 GPa [40]. *Fddd* is a face-centered orthorhombic structure with two atoms per primitive cell located on equivalent sites, with lattice and basis vectors

$$\begin{aligned} \mathbf{A}_1 &= (0, b/2, c/2) \\ \mathbf{A}_2 &= (a/2, 0, c/2) \\ \mathbf{A}_3 &= (a/2, b/2, 0) \end{aligned} \qquad \begin{aligned} \mathbf{b}_1 &= (a/8, b/8, c/8) \\ \mathbf{b}_2 &= (-a/8, -b/8, -c/8) \end{aligned} . \tag{5}$$

Note that the *Fddd* structure is completely symmetric with respect to the *a*, *b* and *c* axes. These axes may be assigned in different ways, so quoted c/a and b/a axial ratios depend on the assignment made. Also, it is often convenient to treat *Fddd* in an equivalent but larger simple orthorhombic unit cell with eight atoms per cell. This is done here for both the phonon spectrum and in all MGPT-MD simulations.

The *Pmma* space group is a close cousin of *Pnma*. This structure was previously found to be a competitive with bcc in a genetic algorithm search for Mo [42]. *Pmma* is a simple orthorhombic structure with four atoms per primitive cell, located on two *inequivalent* sites defined by an internal structural parameter denoted as *z*. The lattice and basis vectors are

$$\begin{aligned} \mathbf{A}_1 &= (a, 0, 0) \\ \mathbf{A}_2 &= (0, b, 0) \\ \mathbf{A}_3 &= (0, 0, c) \end{aligned} \qquad \begin{aligned} \mathbf{b}_1 &= (a/2, b/2, c/2) \\ \mathbf{b}_2 &= (a/4, 0, -z) \\ \mathbf{b}_3 &= (0, b/2, c/2) \\ \mathbf{b}_4 &= (-a/4, 0, z) \end{aligned} . \tag{6}$$

The atom sites defined by $\mathbf{b}_1$ and $\mathbf{b}_3$ are equivalent, as are the sites defined by $\mathbf{b}_2$ and $\mathbf{b}_4$. For $z = 0$ all four sites become equivalent.

The *Cmcm* space group is the observed room-temperature structure of α-U [39]. *Cmcm* is a base-centered orthorhombic structure with two atoms per primitive cell, located on inequivalent sites defined by an internal structural parameter denoted as *y*. The lattice and basis vectors are

$$\begin{aligned} \mathbf{A}_1 &= (a/2, b/2, 0) \\ \mathbf{A}_2 &= (-a/2, b/2, 0) \\ \mathbf{A}_3 &= (0,0,c) \end{aligned} \qquad \begin{aligned} \mathbf{b}_1 &= (0,0,0) \\ \mathbf{b}_2 &= (0, 2y, c/2) \end{aligned} . \tag{7}$$

In MGPT-MD simulations, it is convenient to treat *Cmcm* or α-U in an equivalent but larger simple orthorhombic unit cell with four atoms per cell. Also, because α-U is the more commonly used terminology for the *Cmcm* structure, we will use this terminology in the remainder of this paper.

The detailed arrangement of atoms in each of our four orthorhombic structures for compressed Ta is illustrated in Fig. 2. The important c/a and b/a axial ratios, which define our simple-orthorhombic simulation cells, are both volume and temperature dependent. The behavior of these parameters at both low and high temperature is discussed in Sec. IVA. The remaining internal structural parameters are automatically relaxed in MGPT-MD simulations, and we need only establish $T = 0$ starting values of these parameters from total-energy minimization, which we consider in the next section.

B. $T = 0$ structural phase stability

To examine low-temperature structural phase stability in our four candidate orthorhombic structures, we have calculated optimized MGPT total energies for these structures at $T = 0$ via Eq. (1). In each case E_{tot} has been minimized as a function of atomic volume Ω with respect to the b/a and c/a axial ratios and all internal structural parameters. These results are plotted as total energy differences relative to bcc, $E_{\text{tot}} - E_{\text{bcc}}$, per atom in Fig. 3(a). Also shown for reference in Fig. 3(a) is the corresponding result for the hex-ω structure from Paper I. As a group, the orthorhombic relative total energies are rather tightly clustered and significantly lower in energy than hex-ω. The *Fddd* structure has the lowest total energy of the orthorhombic phases considered down to a volume near 70 a.u., corresponding to pressure of about 300 GPa. At lower volumes and higher pressures

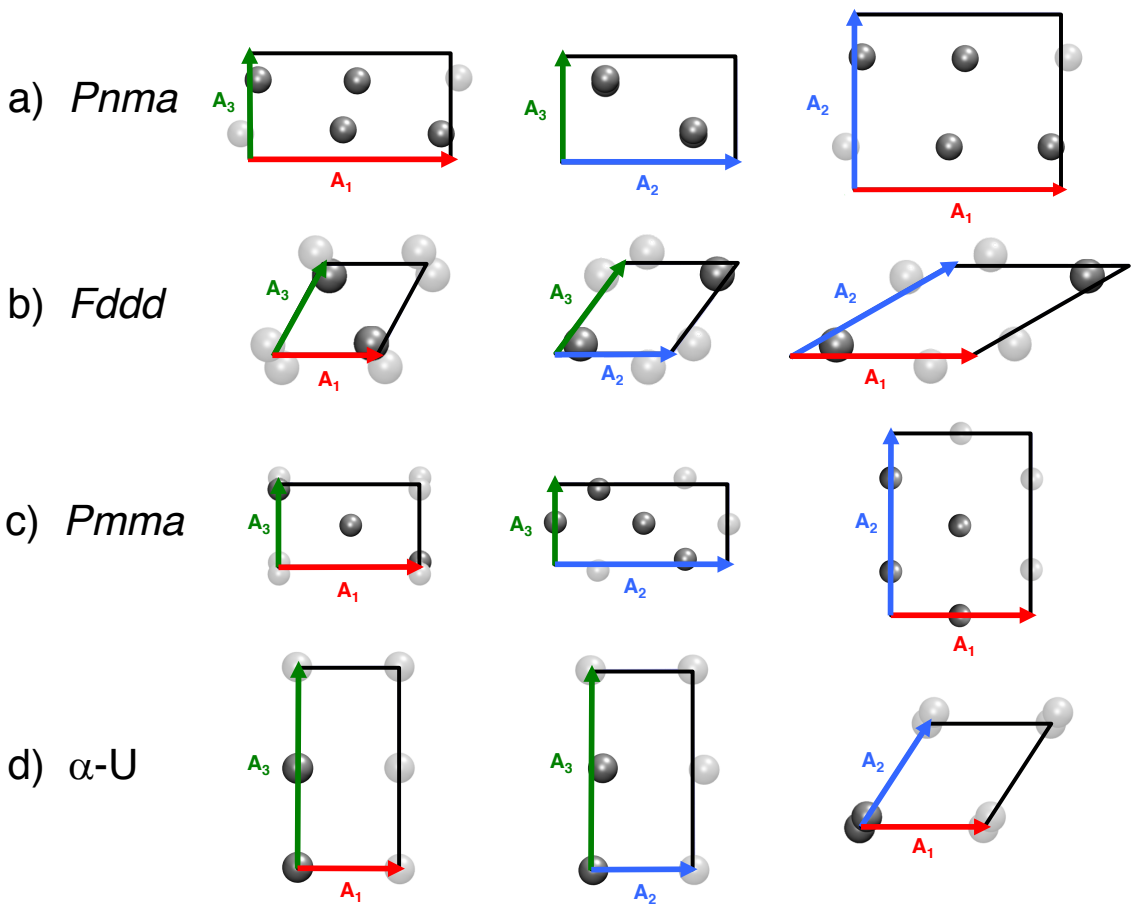

FIG. 2. The four orthorhombic structures of Ta explored in this work, as obtained at conditions of $T = 0$ and $\Omega = 80$ a.u.. The displayed cells are shown normal to the three lattice vectors $\mathbf{A}_1$, $\mathbf{A}_2$, and $\mathbf{A}_3$. The dark atoms compose a particular choice of atomic basis entirely within the cell, while the translucent atoms are periodic images. (a) *Pnma*; (b) *Fddd*; (c) *Pmma*; and (d) α-U (*Cmcm*).

Pmma becomes the lowest-energy structure. In this regard, note that both the *Pmma* and α-U energies peak just above 70 a.u. before turning downward at lower volumes. In the case of *Pmma* at least, this behavior appears to be closely linked to the behavior of its internal *z* parameter, which is shown in Fig. 4. Unlike the internal structural parameters for *Pnma* and α-U, which are nearly constant over the entire volume range in Fig. 3(a), for *Pmma* below 83 a.u., its *z* parameter suddenly and rapidly decreases from a value of about 0.1 above 83 a.u. to zero at 67 a.u. At this point, all four of the atom sites in the *Pmma* structure become equivalent.

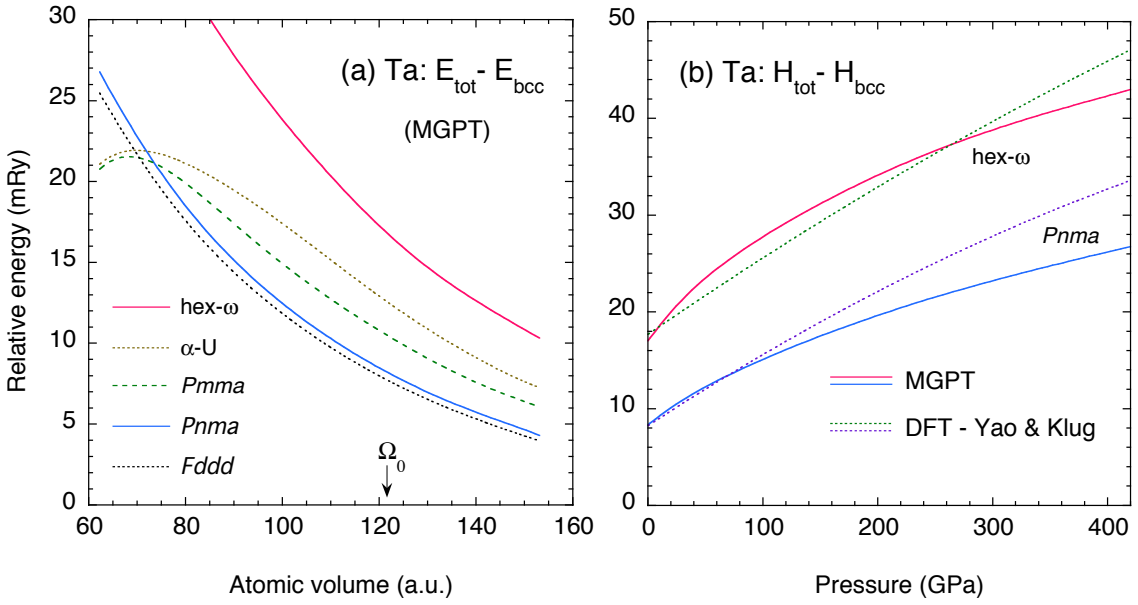

FIG. 3. Optimized MGPT hexagonal and orthorhombic total energies and enthalpies per atom at $T = 0$ relative to bcc. (a) hex-ω, α-U, *Pmma*, *Pnma*, and *Fddd* relative total energies vs. volume, where Ω_0 denotes the observed bcc equilibrium volume; (b) hex-ω and *Pnma* relative total enthalpies vs. pressure, together with the corresponding DFT results of Yao and Klug [15].

One can also convert total energy as a function of volume to total enthalpy as a function of pressure, $H_{\rm tot} = E_{\rm tot} + PN\Omega$. We do this here for the hex-ω and *Pnma* structures for direct comparison with the DFT calculations of Yao and Klug [15]. This comparison is made in Fig. 3(b), in units of enthalpy relative to bcc per atom. At low pressures the MGPT and DFT results agree very well. Above about 250 GPa, the MGPT relative enthalpies trend somewhat below the DFT values, but the agreement remains reasonable up to the maximum $T = 0$ pressure treated here of 420 GPa.

C. Quasiharmonic phonons and Debye temperatures

As discussed in Paper I and in agreement with first-principles DFT calculations [12,43], MGPT Ta is both mechanically and thermodynamically stable in the bcc phase at $T = 0$ over the present pressure range, which extends up to 420 GPa, with real quasiharmonic

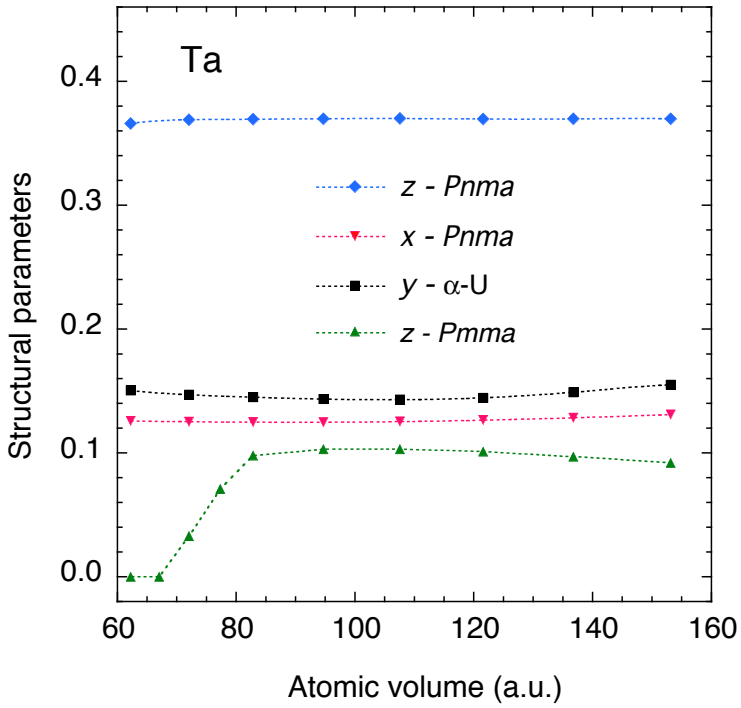

FIG. 4. Optimized internal parameters for the *Pnma*, α-U, and *Pmma* orthorhombic structures at $T = 0$, as used in Fig. 3 for the MGPT total energies and enthalpies.

phonons frequencies calculated throughout the Brillouin zone (BZ) at all volumes. Similarly, the cubic A15 structure was found to be mechanically stable over the same pressure range with real MGPT quasiharmonic phonon spectra calculated at the same volumes. A representative A15 result is plotted here in Fig. 5(a) at $\Omega = 121.6$ a.u. near ambient pressure, a result that qualitatively agrees with the recent DFT calculation of Yao and Klug [15]. In contrast, the other structures considered in Paper I, fcc, hcp, and hex-ω, were all found to be mechanically *unstable* at pressures up to at least 420 GPa, with one or more imaginary phonon branches calculated in each case at all volumes. MGPT phonon spectra for fcc and hcp were plotted in Fig. 6 of Paper I, while a similar result for hex-ω is displayed here in Fig. 5(b). The latter result also qualitatively agrees with the recent DFT calculations of both Yao and Klug [15] and Liu *et al.* [16].

In contrast to *Pnma* and *Fddd*, both *Pmma* and α-U are here predicted to be mechanically unstable up to 420 GPa, with one or more imaginary phonon branches calculated at all volumes in each structure. Interestingly, however, under compression the number of

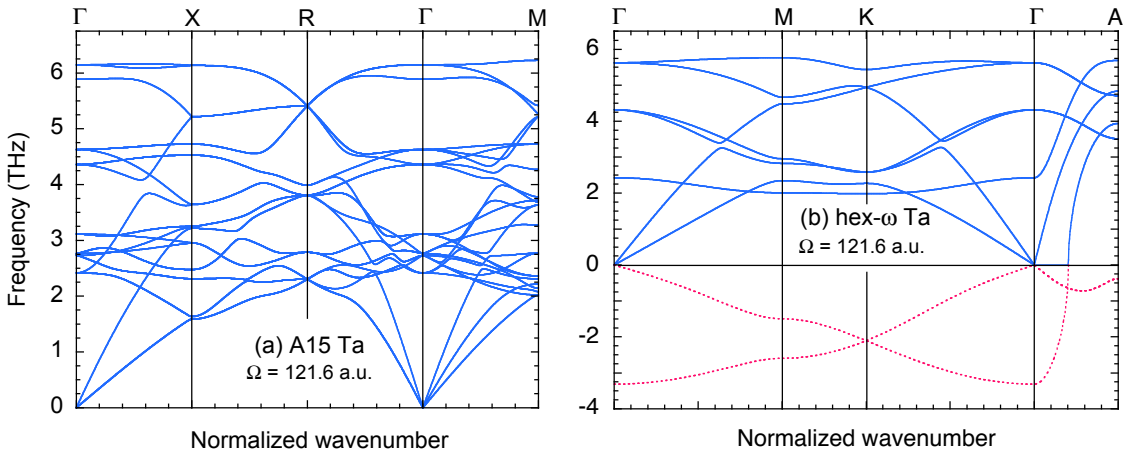

FIG. 5. Representative MGPT quasiharmomic phonon spectra for the A15 and hex-ω structures in Ta, as calculated near ambient pressure at $\Omega = 121.6$ a.u. Real phonon branches are shown as solid lines at positive frequencies. Imaginary phonon branches are displayed as dashed lines at negative frequencies. (a) A15; (b) hex-ω.

phonon frequencies calculated to be imaginary steadily decreases with increasing pressure. The trend suggests that at some higher pressure above 420 GPa both *Pmma* and α-U will eventually become mechanically stable. This trend toward high-pressure mechanical stability is consistent with the downward trending *Pmma* and α-U structural-energy differences with bcc seen in Fig. 3(a) below $\Omega = 70$ a.u.

We have now likewise calculated MGPT quasiharmonic phonon spectra for the four present candidate orthorhombic structures over the 0–420 GPa pressure range of interest. Representative results calculated at $\Omega = 121.6$ a.u. near ambient pressure are shown in Fig. 6. As in the case of bcc and A15, we find the *Pnma* and *Fddd* structures to be mechanically stable over the entire pressure range, with all real phonon frequencies calculated throughout the simple-orthorhombic BZ at all volumes. In the case of *Pnma*, these results qualitatively agree with the DFT calculations of Yao and Klug to 400 GPa [15] and Liu *et al.* to 250 GPa [16]. In the case of *Fddd*, a new mechanically stable phase of Ta is predicted. As we have indicated above, it is convenient here to treat face-centered orthorhombic *Fddd* in an exactly equivalent simple orthorhombic structure, both

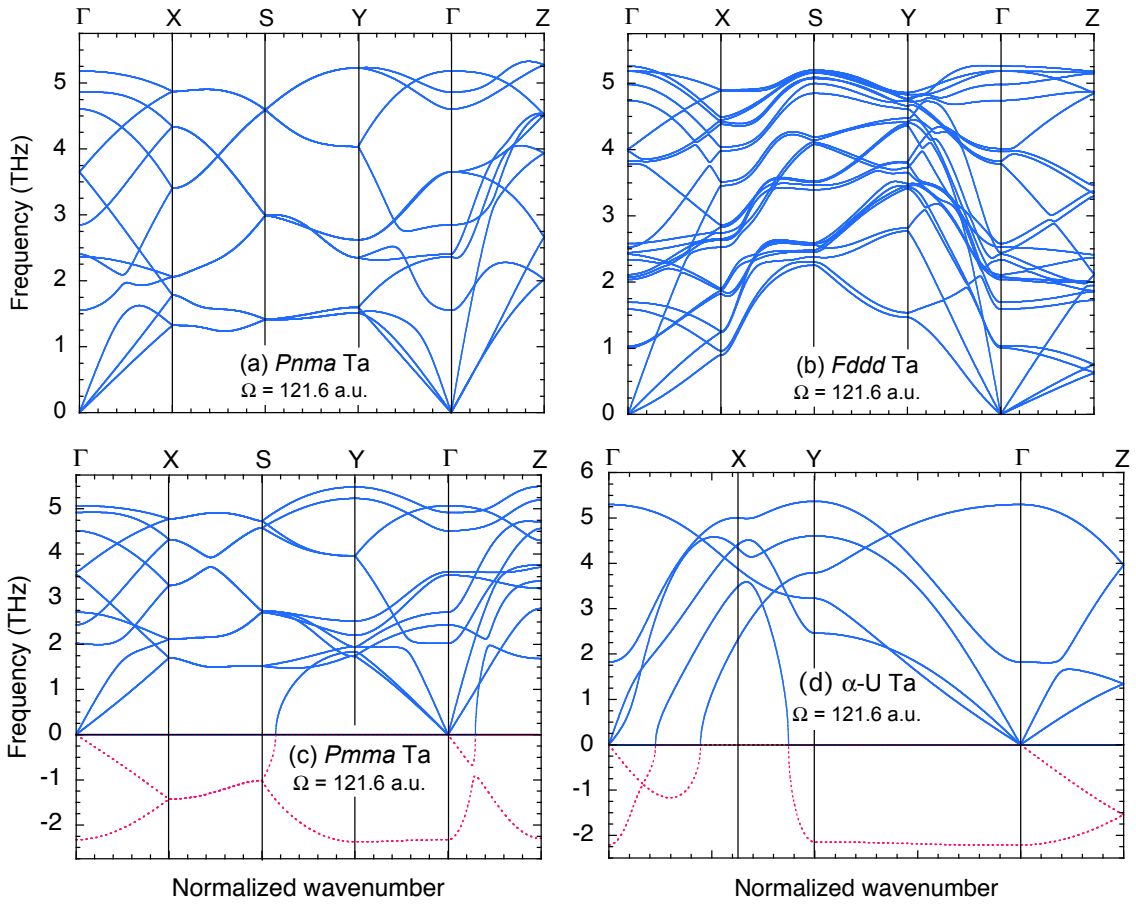

FIG. 6. Representative MGPT quasiharmomic phonon spectra for the present four candidate orthorhombic structures in Ta, as calculated near ambient pressure at $\Omega = 121.6$ a.u. Real phonon branches are shown as solid lines at positive frequencies. Imaginary phonon branches are displayed as dashed lines at negative frequencies. (a) *Pnma*; (b) *Fddd*, here represented as an equivalent simple orthorhombic structure with 8 atoms per unit cell; (c) *Pmma*; and (d) α-U.

in the calculation of $T = 0$ phonons, as in Fig. 6(b), and in subsequent finite-T MD simulations discussed below.

For the four structures we have predicted to be mechanically stable at $T = 0$ below 420 GPa in pressure, namely, bcc, A15, *Pnma*, *and Fddd*, we have also calculated MGPT Debye temperatures as a function of volume. As we have previously done in Ta [14], we define the Debye temperature $\Theta_D(\Omega)$ here as a measure of the average phonon

frequency at volume Ω by the relation

$$k_{\mathrm{B}}\Theta_{\mathrm{D}}(\Omega)=\frac{8}{9}E_{\mathrm{ph}}^{0}(\Omega)\ , \tag{8}$$

where E_{ph}^{0} is the zero-point vibrational energy

$$E_{\mathrm{ph}}^{0}(\Omega)=\frac{1}{2N}\sum_{\mathbf{q},\lambda}h\nu_{\lambda}(\mathbf{q},\Omega)\ , \tag{9}$$

with $\nu_{\lambda}(\mathbf{q},\Omega)$ a frequency of the λ phonon branch at wavevector $\mathbf{q}$ in the first BZ. Converting volume to pressure at $T=0$, we have plotted Θ_{D} as function of pressure in Fig. 7 for the four mechanically stable structures. All four curves are clearly very similar in both shape and magnitude, with bcc having the highest Debye temperature and *Fddd* the lowest at all pressures, but with $\Theta_{\mathrm{D}}(P)$ for *Fddd* nearly the same as that for *Pnma*. We find that the *Fddd* and *Pnma* Debye temperatures are only 3-8% below that of bcc up to 420 GPa.

D. Spontaneous temperature-induced transitions to bcc for *Fddd* and *Pnma*

At low temperatures, one can readily confirm the mechanical stability of the *Fddd* and *Pnma* orthorhombic phases at all volumes of interest though MGPT-MD simulation. Using constant-volume, simple-orthorhombic simulation cells with 512 atoms, these structures exhibit very harmonic lattice vibrations with a thermal energy E_{th} close to $3k_{\mathrm{B}}T$. At the same time, it is clear from Fig. 3(a) that at low temperature there is a large free-energy difference between the metastable *Fddd* or *Pnma* structures and the ground-state bcc structure at all volumes. This free-energy difference results in a large thermodynamic potential favoring bcc, a potential that ranges in magnitude from about 8 mRy near ambient pressure to roughly 26 mRy at 420 GPa. Consequently, in MGPT-MD simulations at a given temperature and volume, the *Fddd* and *Pnma* structures are vibrating harmonically in relatively shallow potentials energy wells separated by a low-lying energy barrier from a much deeper bcc potential energy well. Therefore, if the

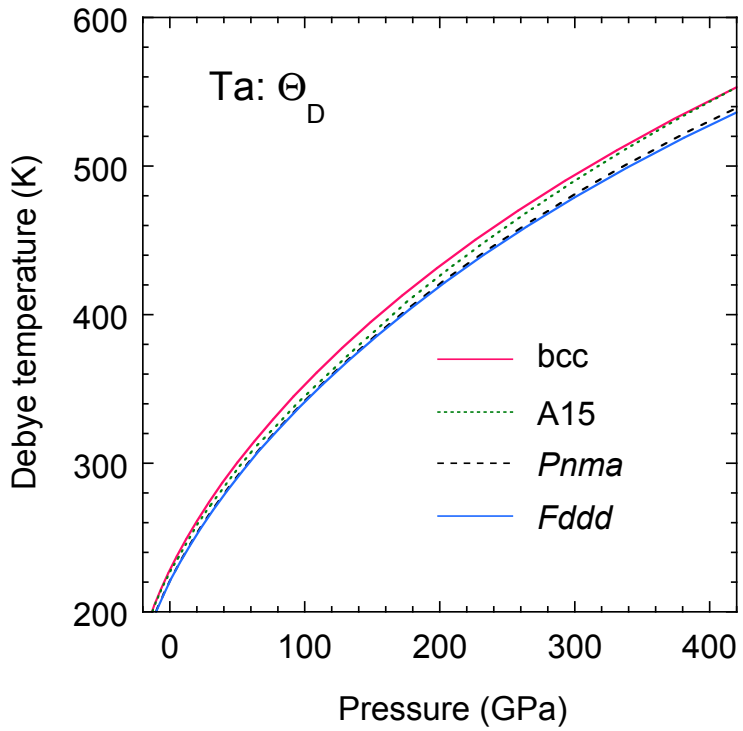

FIG. 7. Calculated MGPT Debye temperatures for the four mechanically stable structures found in Ta up to 420 GPa at zero temperature.

energy barrier for the given orthorhombic structure is not too high, as we confirm below for *Fddd* and *Pnma*, then at some temperature it may be possible to surmount the barrier and transform to the bcc structure.

Such spontaneous temperature-induced $Fddd \rightarrow$ bcc and $Pnma \rightarrow$ bcc phase transitions are indeed observed in MGPT-MD simulations on Ta. Starting at 100 K and slowly increasing the equilibrated temperature at fixed volume, these transitions are quite dramatically revealed in the behavior of the normalized thermal energy $E_{\rm th}(\Omega,T)/3k_{\rm B}T$ of the given orthorhombic structure. This is illustrated in Fig. 8 for *Fddd* and *Pnma* Ta simulated at a compressed volume of 82.9 a.u., corresponding to about 154 GPa in pressure at zero temperature. The bcc nature of the final transformed state is readily confirmed by simultaneously monitoring the radial and angular distribution functions at each equilibrated temperature. Also, as shown in Fig. 8(a) for *Fddd* Ta, there is only a small size dependence in the predicted transition temperature beyond a system size of

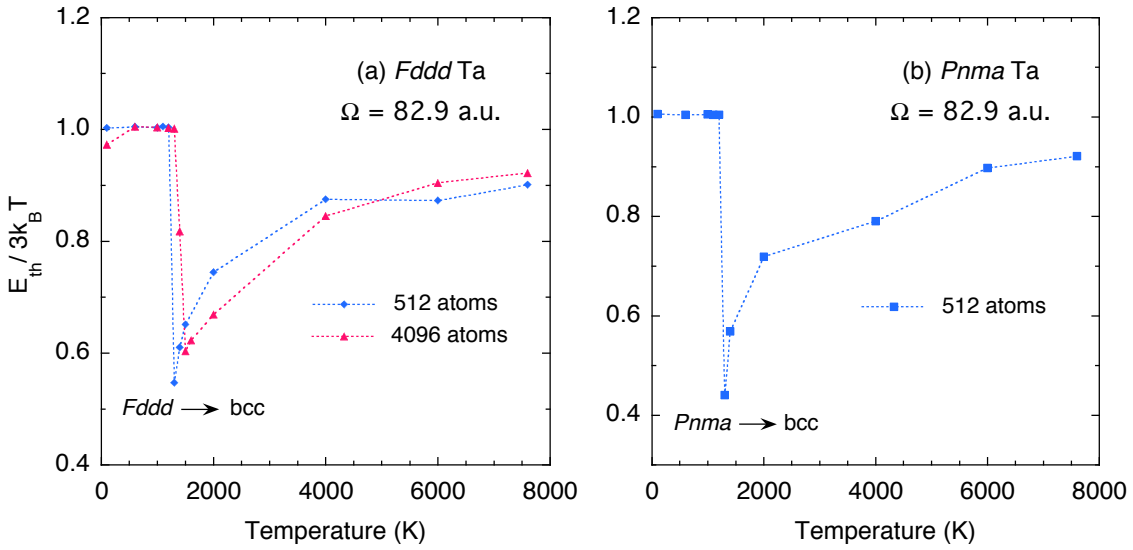

FIG. 8. Normalized thermal energy $E_{\rm th}(\Omega,T)/3k_{\rm B}T$ as a function of equilibrated temperature in the mechanically stable orthorhombic phases of Ta, as obtained from MGPT-MD simulations at $\Omega = 82.9$ a.u., corresponding to a $T = 0$ pressure of 154 GPa. The sharp drop in $E_{\rm th}/3k_{\rm B}T$ indicates a temperature-induced phase transition to bcc. (a) *Fddd* for 512 and 4096 atoms; (b) *Pnma* for 512 atoms.

512 atoms. The absence of any large size dependence here directly reflects the harmonic nature of the *Fddd* and *Pnma* lattice vibrations below 1500 K in Ta.

The predicted temperature-induced $Fddd \rightarrow$ bcc and $Pnma \rightarrow$ bcc transitions occur at all volumes of interest, with transition temperatures ranging from just over 100 K at high pressure above 400 GPa to 1250-1450 K in the 80-150 GPa pressure range, as shown in Fig. 9. Interestingly, the latter peaks in transition temperature turn out to be precursors to the melting behavior we find for *Fddd* and *Pnma*, which will be discussed in Sec. IV. This connection is especially noteworthy because of the very different character of the mechanical stability of these structures at low and high temperature. In sharp contrast to the low-temperature regime, where mechanical stability is fully commensurate with harmonic lattice vibration, with an absence of anharmonic vibration and large size effects on phase transitions, mechanical stability at high temperature in *Fddd* and *Pnma* is strongly influenced by anharmonic vibration, leading to large size effects in the melting. Indeed, it is only the large anharmonic effects at high temperature that allow all of the

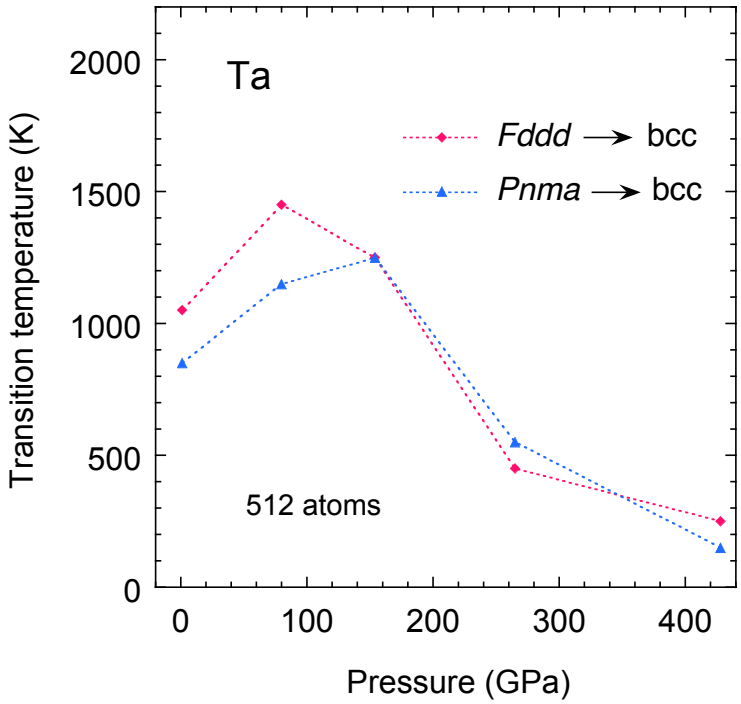

FIG. 9. Predicted $Fddd \rightarrow$ bcc and $Pnma \rightarrow$ bcc phase-transition temperatures in Ta vs. pressure, as obtained from MGPT-MD simulations with 512 atoms.

orthorhombic structures considered here to be created and maintained in equilibrium prior to melting. On the other hand, the fact that the *Fddd* and *Pnma* structures can't be so maintained at intermediate temperatures without a phase transition to bcc thwarts the construction of global free energies in these phases based on a $T = 0$ reference state, as discussed in Sec. V.

Additional insight into the present $Fddd \rightarrow$ bcc and $Pnma \rightarrow$ bcc phase transitions can be obtained from the constant-volume energy landscapes that connect the *Pnma* and *Fddd* structures to bcc. Representative MGPT energy landscapes at $\Omega = 121.6$ a.u., corresponding to a pressure of 1.1 GPa in Fig. 9, are displayed in Fig. 10. In terms of such energy landscapes, the microscopic mechanism allowing the transformation between the *Pnma* and bcc structures has been examined in the work of Yao and Klug [15]. The transformation path can be described by two independent path variables, which are given most simply in terms of the bcc crystal structure. The first variable is a homogeneous deformation of the (110) planes, and the second is a shearing of every other (110) plane

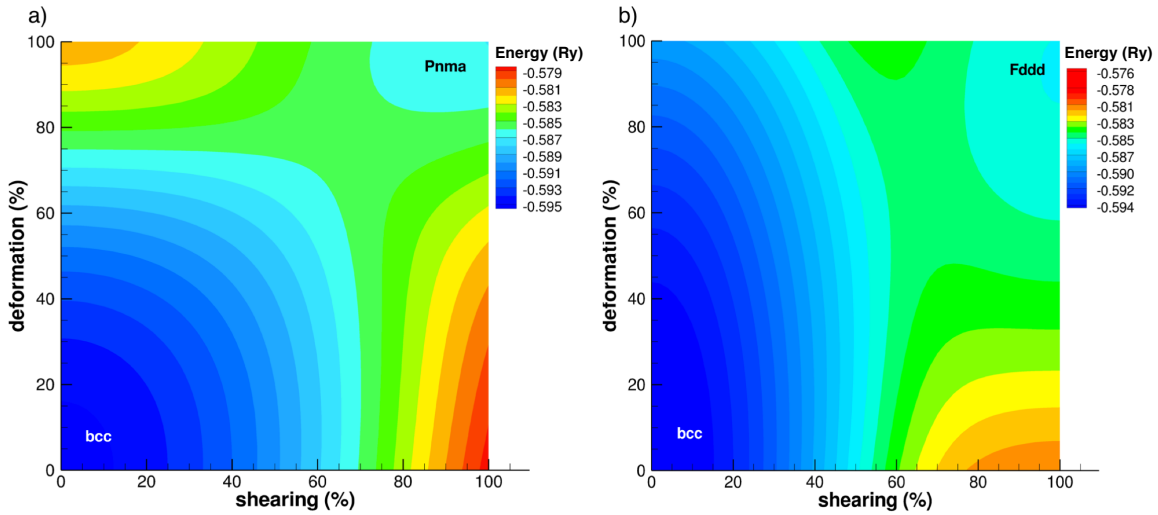

FIG. 10. MGPT energy landscapes for the constant volume transformation between the orthorhombic phases and the bcc phase at $\Omega = 121.6$ a.u. in terms of the homogeneous deformation and shearing of the (110) planes of bcc at 0 K. (a) *Pnma*; (b) *Fddd*.

in the [1-10] direction. The *Pnma*-bcc energy landscape in this shearing-deformation configuration space, as given in Fig. 10(a), shows that the transformation energy barrier relative to bcc is 9.6 mRy and occurs at 75% deformation and 70% shearing. In contrast, the energy barrier relative to *Pnma* is just 1.4 mRy, consistent with the modest calculated $Pnma \rightarrow$ bcc transformation temperature of 850 K shown in Fig. 9.

In a similar manner, the transformation between the bcc and *Fddd* structures can also be described in terms of the homogeneous deformation and shearing of the (110) planes of the bcc structure. The homogeneous deformation is again applied to the (110) planes, while shearing consists of moving every other pair of two consecutive (110) planes in the [10-1] direction. The *Fddd*-bcc energy landscape in shearing-deformation configuration space, as given in Fig. 10(b), shows that the transformation barrier relative bcc is 11 mRy and occurs at 70% shearing and 70% deformation. The energy barrier relative to *Fddd* is then 3.3 mRy, which is qualitatively consistent with the higher calculated $Fddd \rightarrow$ bcc transformation temperature of 1050 K at 1.1 GPa shown in Fig. 9.

IV. HIGH-T MECHANICAL STABILITY and MELT of ORTHORHOMBIC PHASES

In this section, we consider the high-T,P dependence of the structure, mechanical and thermodynamic stability, and melt curves of the orthorhombic phases of Ta. The high-temperature structure is assessed on the basis of *in situ* determination of the volume-dependent c/a and b/a axial ratios near $T = T_m$. The corresponding high-T mechanical stability of a given phase is assessed from the criterion established in Paper I, which is based on the equality of the normal components of the stress tensor. The relative thermodynamic stability of the orthorhombic phases is determined from their melt curves, which are computed as a function of pressure up to 420 GPa. We highlight the prevalence of anharmonic-driven size effects on the melt curves of these phases, size effects which are qualitatively similar, but larger in magnitude, than those found in Paper I for other anharmonic phases of Ta. We then determine final converged melt curves for each orthorhombic structure using large-cell, size-effect-free two-phase MGPT-MD simulations and comment on possible polymorphism.

A. Temperature and volume dependence of c/a and b/a

The phases of Ta examined in Paper I had cell shapes that could be considered fixed and independent of temperature. In contrast, the orthorhombic phases treated here have c/a and b/a axial ratios, as well as internal coordinates, which can vary throughout the temperature and volume space considered. To determine the melts of these phases accurately, the temperature-dependent shape of the unit cell must be resolved, and we have accomplished that task here at $T = T_m$ for each melting volume considered. As indicated above in connection with Fig. 3, the corresponding $T = 0$ primitive cells are determined by simply minimizing the *total energy* as a function of volume. At $T = T_m$, however, one must minimize the local *free energy* with respect c/a and b/a under the conditions of constant volume and high temperature. Here, we do this by performing short MGPT-MD simulations at a given volume and temperature to obtain an average stress tensor. The cell is adjusted iteratively until the normal stresses from the calculated stress tensor are equivalent. In this way, the temperature-dependent cell shape at $T = T_m$ is mapped out across volume space.

The volume dependence of the c/a and b/a axial ratios for the *Pnma* and *Fddd* structures at both low and high temperature is shown in Fig. 11. At $T = 0$, where both structures are mechanically stable, the c/a ratio of *Pnma*, as given in Fig. 11(a), is relatively constant with respect to volume, while the c/a ratio of *Fddd*, as given in Fig. 11(b), increases with increasing volume. These trends are relatively unchanged at $T = T_m$. The primary influence of temperature in both cases is to increase the magnitude of c/a, with the exception of *Fddd* at low volumes below 85 a.u. (corresponding to pressures above 135 GPa). At $T = 0$, the b/a ratio shows a slight decrease with increasing volume in *Pnma*, as given in Fig. 11(c), and a slight increase with volume in *Fddd*, as given in Fig. 11(d). Along the melt curve, the b/a ratio in *Pnma* becomes less sensitive to volume, though that of the *Fddd* structure maintains its $T = 0$ behavior to increase with increasing volume. As with the c/a ratio, the b/a ratio is generally larger at $T = T_m$ than at $T = 0$.

The corresponding volume dependence of the c/a and b/a axial ratios in the *Pmma* and α-U structures at low and high temperature is given in Fig. 12. At $T = 0$, where both structures are mechanically *unstable*, the c/a ratio of *Pmma*, as shown in Fig. 12(a), is relatively constant, while that of α-U, as shown in Fig. 12(b), decreases with increasing volume. At $T = T_m$, the c/a ratio for both of these systems is relatively constant and smaller compared to the $T = 0$ values. At $T = 0$, the b/a ratio of both *Pmma*, as given in Fig. 12(c), and α-U, as given in Fig. 12(d), exhibit a convex, parabolic behavior with respect to volume increase, and in both cases display a maxima between 100-120 a.u. Along the melt curve, the b/a ratio of both phases becomes insensitive to volume. Also, unlike the c/a ratio, the b/a ratio of both structures increases with rising temperature.

Overall, the influence of volume on the c/a and b/a ratios of the orthorhombic phases near the melting temperature is weak. The only structure that appreciably changes as a function of volume is *Fddd*, though the largest changes across the examined volume range occur for the c/a ratio and are on the order of 6%. The weak volume dependence

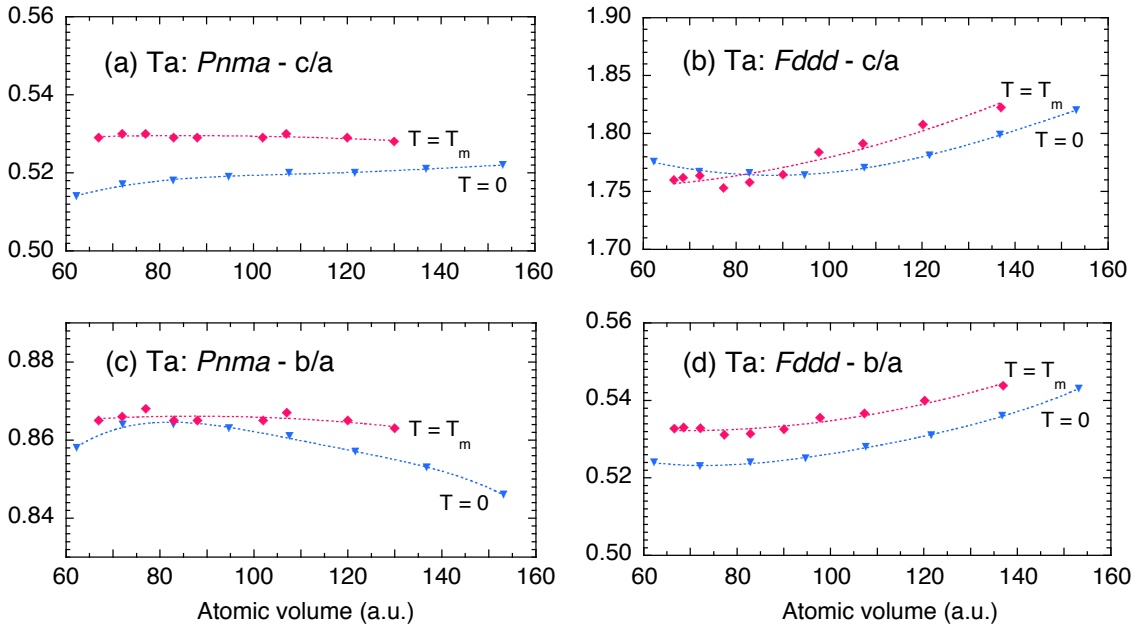

FIG. 11. Volume dependence of the c/a and b/a axial ratios for the *Pnma* and *Fddd* structures in Ta, as calculated at $T=0$ from MGPT total-energy minimization, and at $T=T_m$ from free-energy minimization using MGPT-MD simulations with supercells composed of $10\times10\times10$ simple-orthorhombic unit cells, containing 4000-8000 atoms. (a) c/a for *Pnma*; (b) c/a for *Fddd*; (c) b/a for *Pnma*; (d) b/a for *Fddd*.

actually simplifies the determination of the melt curve in the *Pnma*, *Pmma*, and α-U structures by allowing us to treat the shape of the orthorhombic unit cell as constant near the melt temperature.

B. Mechanical stability near melt

Testing of mechanical stability in MD simulations can be accomplished through *in situ* calculation of the stress tensor σ. A signature of mechanical stability in a dynamical system is equivalent diagonal, or normal, σ_{ii} components (*i.e.*, $\sigma_{11}=\sigma_{22}=\sigma_{33}$), and negligible off-diagonal, or shear, σ_{ij} components. As was done in Paper I, in our present MGPT-MD simulations we quantify the first of these conditions with the parameter $\delta\sigma$, which describes the deviation of the normal stresses from the pressure:

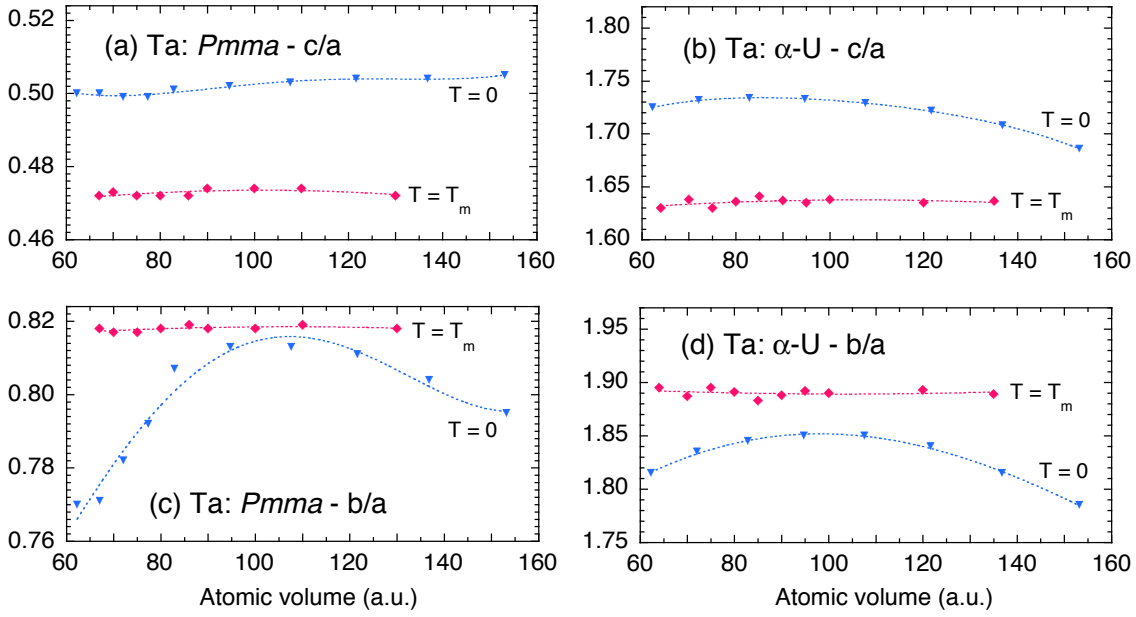

FIG. 12. Volume dependence of the c/a and b/a ratios for the *Pmma* and α-U structures of Ta at $T = 0$ and $T = T_m$, calculated as in Fig. 11. (a) c/a for *Pmma*; (b) c/a for α-U; (c) b/a for *Pmma*; (d) b/a for α-U.

$$\delta\sigma = \sqrt{(\sigma_{11}^2 + \sigma_{22}^2 + \sigma_{33}^2)/P^2 - 3}\ , \tag{10}$$

where pressure is related to the stress tensor through $P = -(\sigma_{11} + \sigma_{22} + \sigma_{33})/3$. The second condition can be represented by the deviation of the shear stresses from zero, but this measure is often negligible at high temperature, leading to our consideration of $\delta\sigma$ as the primary measure of mechanical stability.

In our studies in Paper I, we found an approximate dividing line of $\delta\sigma = 0.04$ between good to excellent mechanical stability, $\delta\sigma \ll 0.04$, on the one hand, and fair to poor mechanical stability, $\delta\sigma \gg 0.04$, on the other hand, with the latter implying the onset of mechanical *instability*. The present calculated values of $\delta\sigma$, as given in Fig. 13, indicate that the orthorhombic structures here mostly exhibit excellent mechanical stability near $T = T_m$ across the 64 to 135 a.u. atomic volume range. The primary exceptions to this trend are the *Pnma* and *Fddd* structures at large volume, which show sharp upticks in $\delta\sigma$ with increasing volume. This behavior is especially marked in *Fddd* above 110 a.u.,

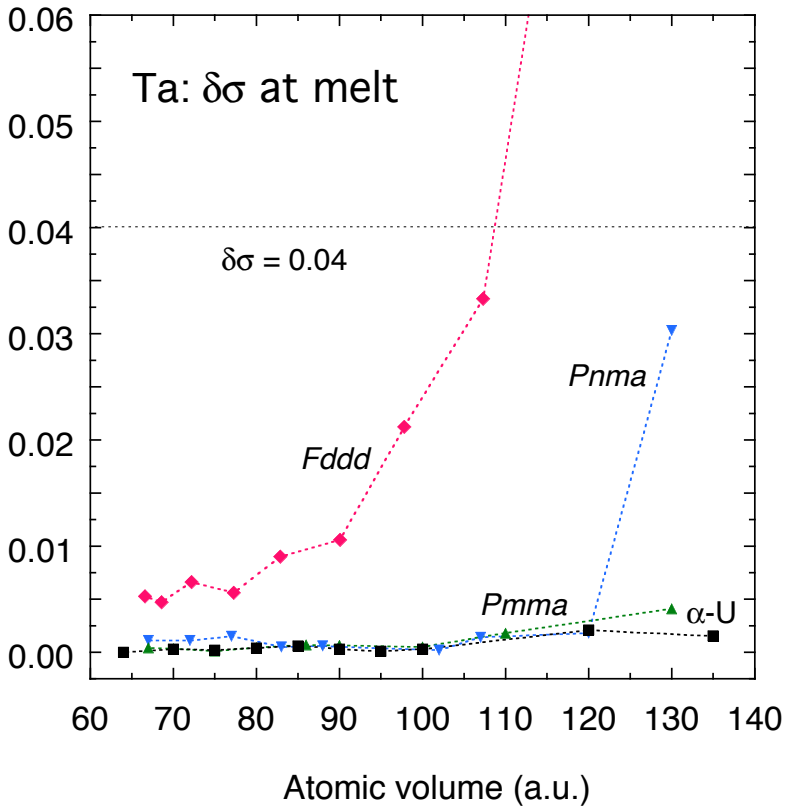

FIG. 13. Volume dependence of the mechanical stability parameter $\delta\sigma$ at the melt temperature for the *Fddd*, *Pnma*, *Pmma*, and α-U orthorhombic structures of Ta, as obtained from MGPT-MD simulations using $10\times10\times10$ supercells (4000-8000 atoms).

corresponding to pressures below about 40 GPa, where $\delta\sigma$ is an order of magnitude larger than that of the other calculated values. The increase in $\delta\sigma$ for *Pnma* , on the other hand, only begins near 120 a.u., corresponding to pressures below 15 GPa, and is not as dramatic as that for *Fddd*, though at volumes larger then 130 a.u. the increase in the *Pnma* values of $\delta\sigma$ will likely continue. Although the rapid increase in $\delta\sigma$ for the *Fddd* and *Pnma* structures foreshadows the onset of high-temperature mechanical instability, this behavior occurs at sufficiently low pressures that it does not significantly impact our calculation of the high-pressure melt curve in either case.

The physics of the decreasing mechanical stability of both *Pnma* and *Fddd* at large values of atomic volume could be related to the mid-temperature thermodynamic instability of these structures noted in Figs. 8 and 9. These phases were shown to transform to bcc at

relatively higher temperatures when the pressure is low. At temperatures beyond the transition temperature to bcc, the *Pnma* and *Fddd* orthorhombic structures only gradually regain metastability, as high-T anharmonic effects arise and grow. The low-pressure orthorhombic to bcc transition is closer in temperature to the melt than that at high pressure, so the anharmonic effects that help stabilize both *Pnma* and *Fddd* near melt may not be fully in play at the lowest pressures.

C. Large anharmonic thermal energies and melt size effects

One can address the degree of vibrational anharmonicity in a given phase directly in our MGPT-MD simulations. The phonon-phonon interactions near melt that fully stabilize phases with either soft or imaginary quasiharmonic phonons can be characterized at high-T,P conditions by the apparent amount of anharmonicity displayed in appropriate thermodynamic functions. Specifically, we can define a simple but useful percentage measure of anharmonicity in a given phase, Q_{ah}, by the relation

$$Q_{\rm ah}(\Omega,T) = 100[1 - E_{\rm th}(\Omega,T)/3k_{\rm B}T] \ , \qquad (11)$$

where $E_{\rm th} = E_{\rm tot} - E_0$ is the thermal energy of the system in that phase, with $E_{\rm tot}$ the total internal energy. In the quasiharmonic limit at high temperature with $A_{\rm el} = E_{\rm el} = 0$, $E_{\rm th} \to 3k_{\rm B}T$ and $Q_{\rm ah} \to 0$.

The calculated values of Q_{ah} near the melt temperature are similar and large, in the range 10-25%, for all the present orthorhombic structures, as shown in Fig. 14. With increasing volume, the anharmonic energy decreases for the *Fddd* and *Pnma* structures and increases for the *Pmma* and α-U structures. At the largest volumes, the *Fddd* and *Pnma* structures have the lowest values of Q_{ah} near 10%. This is qualitatively consistent with their trend toward decreasing mechanical stability at large volume, as discussed above in connection with Fig. 13. At the same time, in comparison to the cubic and hexagonal structures investigated in Paper I, the orthorhombic structures examined here are significantly more anharmonic, with the exception of the hex-ω structure for low values of c/a, which has comparable anharmonicity.

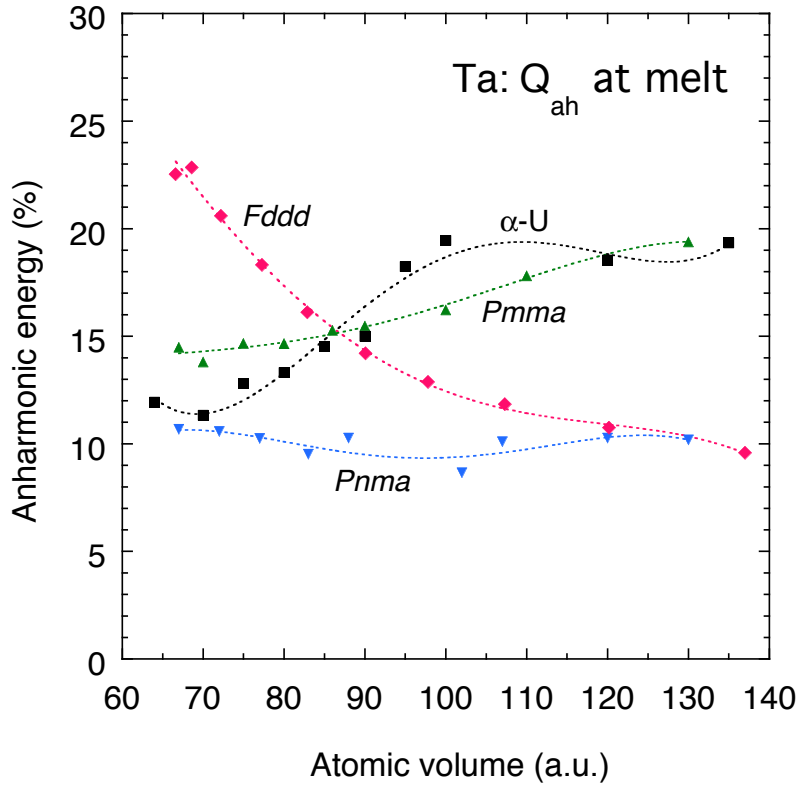

FIG. 14. Dependence of the anharmonic thermal energy Q_{ah} on volume at $T = T_m$ for the *Pnma*, *Fddd*, *Pmma*, and α-U orthorhombic phases of Ta, as obtained from MGPT-MD simulations on $10 \times 10 \times 10$ supercells (4000-8000 atoms).

Both a low $T = 0$ total internal energy and high vibrational anharmonicity and are key factors that help make a given structure thermodynamically competitive at high temperature. As was shown in Paper I, the bcc and A15 structures of Ta are only weakly anharmonic at melt (with $Q_{ah} \sim 0.1\%$ and $\sim 2\%$, respectively), but have the lowest and next lowest $T = 0$ internal energies, which establishes their intrinsic advantage. In contrast, the fcc and hcp phases were found in Paper I to be significantly anharmonic (with $Q_{ah} \sim 5 - 10\%$ at melt), but at the same time, with very high $T = 0$ internal energies. The mechanically stable hex-ω structure with $c/a = 0.53$ was found to be the most anharmonic of the cubic and hexagonal structures considered in Paper I, with values of $Q_{ah} \sim 10 - 30\%$ at melt, but also with a very large $T = 0$ total internal energy. As we have noted in Fig. 3, the $T = 0$ total energies of the present orthorhombic structures

relative to bcc are much smaller than those for hex-ω. Thus with relatively low $T = 0$ internal energies and high vibrational anharmonicity, the orthorhombic structures become very promising candidates for polymorphism in Ta.

In addition to the large magnitude of the high-temperature anharmonic energy possessed by hex-ω and the orthorhombic phases of Ta, one can also anticipate a large spatial extent of the anharmonic effects needed to stabilize these structures near melt. Quantum mechanics tells us that the interatomic forces in metals are long ranged, and this is especially so in complex transition metals like Ta with its strong multi-ion interactions driven by the *d* electrons. This long-range behavior is fully captured by our quantum-mechanical multi-ion MGPT potentials. Unlike the case in semiconductors and insulators, where the interaction range is much shorter and anharmonic effects are often linked to short-range optical vibrational modes, anharmonic effects in metals are linked to very long-range acoustic vibrational modes. This can be appreciated by looking at the quasiharmonic phonon spectra for hex-ω in Fig. 5(b) and for *Pnma* and the other orthorhombic structures in Fig. 6. In all cases there are prominent soft and/or imaginary vibrational modes in acoustic branches. Thus at high temperature the anharmonic vibrational effects that stabilize these structures must have a strong long-ranged acoustic component. This acoustic component is necessarily collective in nature and could easily involve many hundreds or even a few thousands of atoms. Thus large melt size effects extending to a similar number of atoms are physically reasonable and not even surprising for the strongly anharmonic phases in Ta.

In Paper I, we showed that the large anharmonicity of the hex-ω structure was indeed closely associated with a size-dependent melt curve. This in turn leads to the erroneous prediction of the thermodynamic stabilization of hex-ω with respect to bcc when small simulation cells are used in Z-method melt calculations. However, for sufficiently large simulation cells this prediction is reversed. In particular, for the hex-ω structure with $c/a = 0.53$, the MGPT-MD Z-method melting becomes size independent with a uniform $6 \times 6 \times 6$ supercell containing 648 atoms. In direct comparison, our calculated MGPT-

MD Z-melt curve for the present *Pnma* structure becomes size independent with a uniform $7\times7\times7$ simple orthorhombic cell containing 1372 atoms.

In the case of the *Pnma* structure, the threshold for size-independent Z-method melting can be reduced somewhat by using a shape-corrected simulation cell that accounts for the small c/a ratio (0.52-0.54) by keeping the supercell edges of similar length. The use of such a shaped-corrected supercell also appears to have been done by Burakovsky *et al.* in their QMD Z-melt study [19]. In our present MGPT-MD Z-melt size-effect studies on *Pnma*, we have considered shape-corrected simulation cells ranging from $4\times4\times7$ (448 atoms) to $8\times8\times14$ (3584) atoms. Our results indicate that Z-melt size effects become negligible starting with a $5\times5\times9$ (900 atoms) supercell, at which point the calculated *Pnma* melt curve lies entirely below that of bcc, as shown in Fig. 15(a). In sharp contrast, for the two smallest cells we have examined, $4\times4\times7$ (448 atoms) and $4\times4\times8$ (512 atoms), the *Pnma* melt curve crosses above that of bcc at about 290 GPa and 350 GPa, respectively, as also shown in Fig. 15(a). The latter behavior is qualitatively consistent with the QMD Z-melt simulation result of Burakovsky *et al.* [19], displayed in Fig. 15(b), where the *Pnma* melt curve crosses above bcc at about 200 GPa. The exact size and shape of the QMD simulation cell was not stated in Ref. 19, but was only characterized there as a simulation on the order of 500 atoms.

As we have elaborated in detail in Paper I, the simplified and efficient Z-melt method is useful to obtain qualitative trends and approximate lower-bound estimates of melt size effects, but the absolute accuracy of the converged melt curves obtained is often inadequate for the reliable prediction of relative phase stability. In the present context, we know from Paper I that the MGPT-MD Z-melt curve for bcc shown in Fig. 15(a) lies about 200 K too high in temperature, while, as we now demonstrate with accurate two-phase simulations, the converged *Pnma* Z-melt curve is some 500–1000 K too low. At the same time, reliable use of our two-phase melt method for the present orthorhombic structures generally requires larger simulation cells because of the need to achieve full thermodynamic equilibrium in the melting process. The smallest uniform cell for *Pnma* that can be used in our two-phase melt procedure is a $6\times6\times6$ simple orthorhombic cell containing 864 atoms, which is the approximate cell size for which mechanical stability

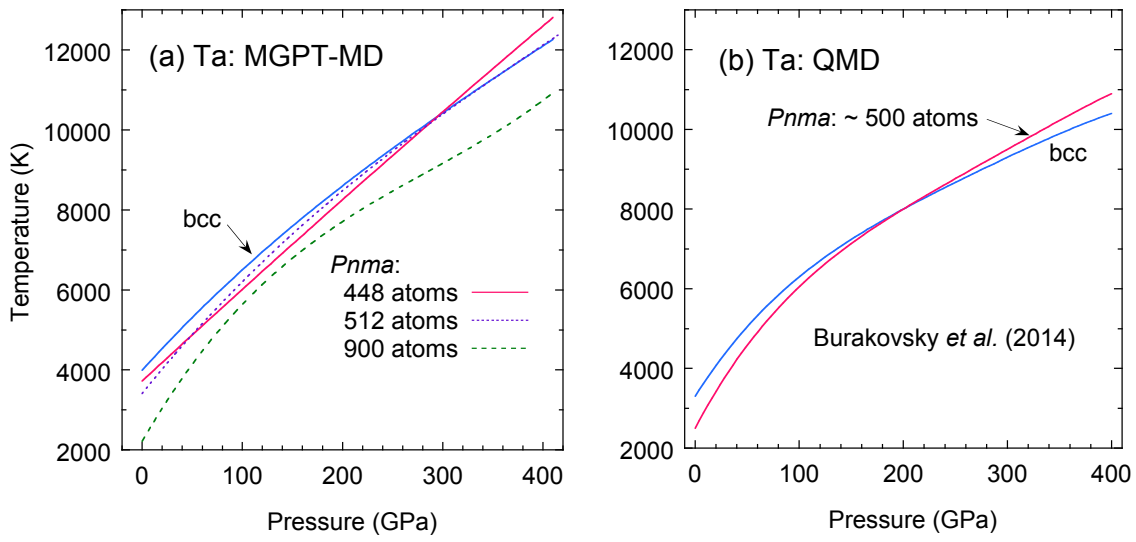

FIG. 15. Size dependence of the *Pnma* melt curve of Ta, compared to the converged bcc melt curve, as obtained by Z-method melt simulations. (a) Present MGPT-MD melt results from 448-, 512- and 900-atom *Pnma* simulations, using shape-corrected $4\times4\times7$, $4\times4\times8$ and $5\times5\times9$ simulation cells, respectively; (b) Previous QMD melt results from ~ 500-atom *Pnma* simulation of Burakovsky *et al.* [19].

of *Pnma* is achieved. As illustrated in Fig. 16, the use of this sized cell produces a *Pnma* melt curve that crosses above the bcc melt curve between 50-100 GPa, and is thus qualitatively similar to the ~ 500 atom Z-melt results given in Fig. 15. Increasing the *Pnma* cell size above $6\times6\times6$ lowers the high-pressure melt curve until one reaches full thermodynamic equilibrium and convergence with a much larger $10\times10\times10$ cell, corresponding to 4000 atoms. The converged *Pnma* curve then lies entirely at or below that of bcc all the way up to 420 GPa, as also shown in Fig. 16, but indeed is much closer to the bcc melt curve than for the Z-melt result shown in Fig. 15(a). It is possible that the two-phase convergence of the melt curve could be obtained with a 30-40% smaller shape-corrected cell, but this issue has not been pursued since only an upper bound is needed here. The size effects displayed in Figs. 15 and 16 support the general conclusion that anharmonic effects strongly impact melt for the present orthorhombic structures, requiring solid-phase simulation cells of up to 4000 atoms to achieve an accurate size-independent melt curve. To ensure full convergence in the final orthorhombic melt curves, we have, in fact, used even much larger solid-phase supercells containing on the

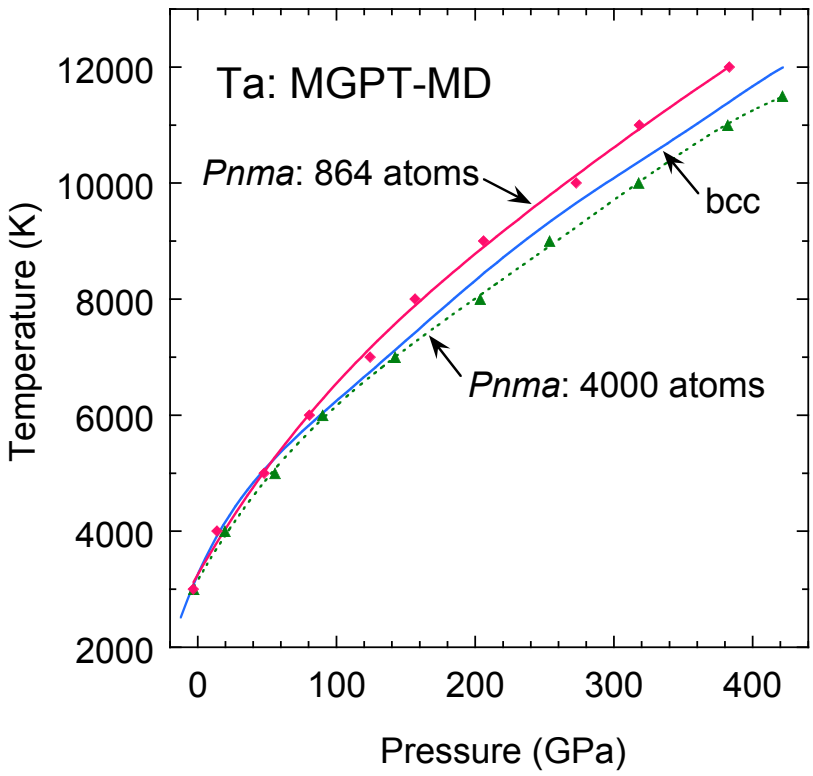

FIG. 16. Size dependence of the *Pnma* melt curve of Ta, as obtained by the present two-phase MGPT-MD 864- and 4000–atom melt simulations, using uniform $6\times6\times6$ and $10\times10\times10$ simulation subcells, respectively. The 864-atom simulation represents the approximate minimum solid cell size for which mechanical stability of *Pnma* is achieved, but not as yet full thermodynamic equilibrium, which is only first achieved in the 4000-atom cell.

order of 40,000 atoms in the two-phase MGPT-MD melt simulations, as described in the next section.

D. Large-cell melt curves and comparison with bcc

To establish the relative thermodynamic stability of the orthorhombic phases of Ta compared to bcc as accurately as possible, we have computed final MGPT-MD two-phase melt curves using very large supercells. To ensure that the melt curves have no anomalous size effects, for the *Pnma, Pmma*, and α-U structures we have used a solid-phase $22\times22\times22$ simple orthorhombic supercell, with a 4-atom basis and 42,592 total

atoms. For the *Fddd* structure, on the other hand, where $c/a \gg b/a$, we have used instead an alternate $16 \times 32 \times 10$ simple orthorhombic supercell to better accommodate the unit cell shape, with an 8-atom basis and 40,960 total atoms. The ~ 40,000-atom cell size was shown in Paper I to lead to highly converged melt curves for the cubic and hexagonal structures, including for the highly anharmonic hex-ω structure. While the melt curve of the baseline bcc structure is size independent beyond 250 atoms, for consistency in the comparisons shown below in Figs. 17 and 18, we have used a $27 \times 27 \times 27$ simple cubic cell for bcc, with a 2-atom basis and 39,366 total atoms, as was done in Paper I.

The high-pressure melt curves for the *Pnma* and *Fddd* structures to 420 GPa, with comparison to bcc, are given in Figs. 17(a) and 17(b), respectively. The melts of these two orthorhombic phases were found to be generally well behaved except at pressures below 50 GPa, where a significant degree of fluctuation was observed in the order parameter used in the two-phase method to determine melt. This effect can likely be attributed to the loss of full mechanical stability noted in Fig. 13 for these phases at the low-*P* melting temperatures. The *Pnma* melt curve is seen to lie below that of bcc across most of the examined pressure range, except at around 90 GPa. At this pressure the *Pnma* melt curve touches the bcc melt curve. The *Pnma* melt curve does not overtake bcc at this point, but instead exhibits a change in slope and remains about 150-450 K below the bcc melt curve for pressures greater than 150 GPa. Similarly, the *Fddd* melt is below the bcc melt across the majority of the pressure range. However, in the interval 100-150 GPa, the melt temperatures of *Fddd* match those of bcc. After this point, the melt curve of *Fddd* also exhibits a decrease in slope and remains roughly 250 K below that of bcc for pressures greater than 200 GPa.

The corresponding large-cell melt curves for the *Pmma* and α-U structures are given in Figs. 18(a) and 18(b), respectively, for pressures up to 420 GPa. The *Pmma* melt is seen to lie below that of bcc across the entire pressure range. Unlike the *Pnma* and *Fddd* phases, the melt curve of *Pmma* does not touch the bcc melt curve at any point, with the melt temperature some 500-1000 K below that of bcc above 100 GPa. The melt curve of α-U is much closer to bcc, but also lies below it across most of the pressure range. Like

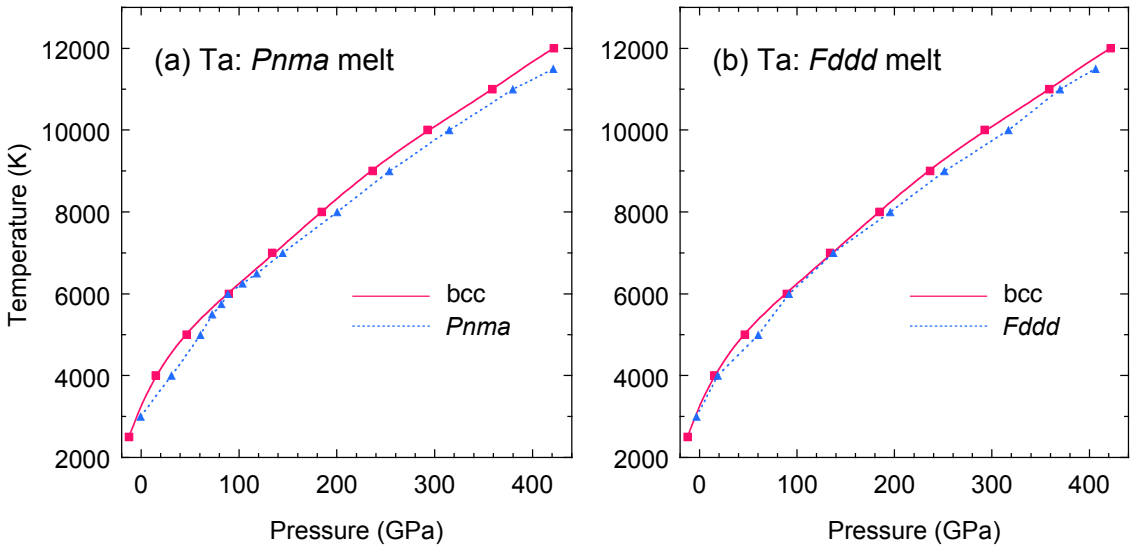

FIG. 17. High-pressure melt curves for the *Pnma* and *Fddd* Ta orthorhombic phases compared with that of bcc, as obtained from MGPT-MD two-phase simulations using large supercells. (a) *Pnma*; (b) *Fddd*.

the *Pnma* and *Fddd* melt curves, the α-U curve touches the bcc curve around 90 GPa. After this point, the melt curve of α-U exhibits a decrease in slope and remains 150-350 K below bcc for pressures greater than 150 GPa.

To confirm the reliability of our two-phase orthorhombic melt curves, we have also done a detailed error analysis on the results. In our two-phase method, a melt pressure P_m on the melting curve is calculated for a chosen melt temperature T_m. Specifically, for each input T_m, the corresponding P_m here has been determined from an ensemble of two-phase simulations that span a small atomic volume range of the solid. The evolution of each of these trial systems was tracked via a short-range order parameter that is discussed in Paper I. During the course of each two-phase simulation, an increasing order parameter indicates crystallization of the liquid, and a decreasing order parameter indicates melt of the crystal. The exact melting volume and pressure was determined by interpolating between the smallest volume that showed crystallization and the largest volume that showed melt. The error in the melt pressure was then determined by the pressure difference at these volumes. In this regard, a 0.5 a.u. volume spacing was used

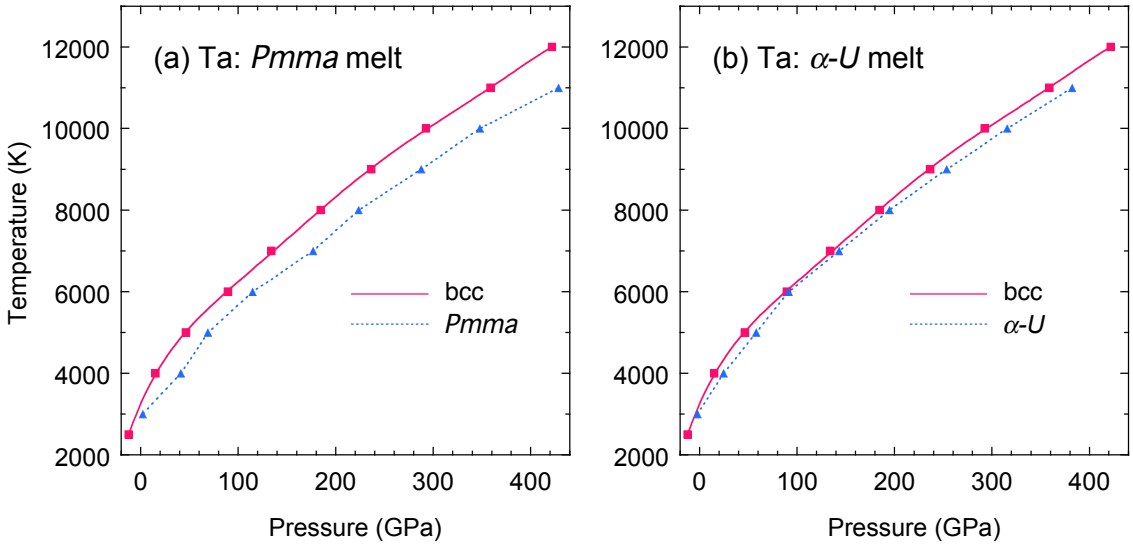

FIG. 18. High-pressure melt curves for the *Pmma* and α-U Ta orthorhombic phases compared with that of bcc, as obtained from MGPT-MD two-phase simulations using large supercells. (a) *Pmma*; (b) α-U.

in this process to determine the melt pressure P_m. The maximum pressure error along the melt curve can then be gauged by the pressure change resulting from changing the melt volume by the spacing value. The maximum pressure error so obtained from an average over the four orthorhombic phases studied here ranges from about 1 GPa at 3000 K near ambient pressure, to 2 GPa at 6000 K near 100 GPa in pressure, to 6 GPa at 9000 K near 250-300 GPa in pressure, to 8 GPa at 11,000-12000 K near 400 GPa in pressure. At 100 GPa and above, this error corresponds to about 2% of the computed melt pressure, which ensures that the noted differences in melt behavior among the four orthorhombic phases are statistically significant. Corresponding maximum temperature errors are calculated to be 30 K at ambient pressure, 63 K at 110 GPa, 99 K at 250 GPa and 163 K at 400 GPa.

Compared to the previous anharmonic cubic and hexagonal Ta phases examined in Paper I, the melt temperatures of three of the four orthorhombic structures studied here are considerably closer to bcc over a wide pressure range. The $c/a = 0.53$ hex-ω melt was shown in Paper I to be some 6000 K below the bcc melt, while the hcp and fcc melt temperatures were found to be on the order of 1000 K below bcc. For the *Pnma*, *Fddd*,

and α-U orthorhombic structures, on the other hand, high-pressure melt temperature differences with bcc are everywhere less that 500 K, indicating a much greater degree of thermodynamic stability. Moreover, the convergence of the *Pnma*, *Fddd*, and α-U melt with the bcc melt around 90-150 GPa suggests that these phases could possibly coexist with bcc inside that pressure range, even if they never become the thermodynamically favored structures.

V. GLOBAL FREE ENERGIES of SELECTED STRUCTURES

Finally, in this section we consider the construction of total Helmholtz free energies $A_{\rm tot}(\Omega,T)$ for the mechanically stable A15, *Pnma*, and *Fddd* phases of Ta, using the RSMD methodology developed in Ref. [14] and there applied to the bcc, fcc, and liquid phases of Ta. In the case of the A15 structure, it is possible to obtain the free energy starting from a $T=0$ reference state, in an analogous manner to that used in Ref. [14] for the bcc structure. In the cases of *Pnma* and *Fddd*, on the other hand, the spontaneous $Pnma \rightarrow$ bcc and $Fddd \rightarrow$ bcc phase transitions at low and intermediate temperatures does not allow the required RSMD temperature integrations from $T=0$ to the vicinity of melt. In these latter cases, we have found it possible to use instead a $T=T_{\rm m}$ reference state based on the corresponding two-phase melt data, in the same manner used in Ref. [14] for the mechanically unstable fcc structure.

A. A15 with $T=0$ reference

For the A15 structure we have proceeded directly from Eq. (2) and calculated $A_{\rm tot}(\Omega,T)$ in terms of its cold, ion-thermal, and electron-thermal components. As in the case of the bcc structure, the ion-thermal component has been obtained in turn as sum of separate, but well-defined quasiharmonic and anharmonic contributions:

$$A_{\rm ion}(\Omega,T) = A_{\rm ion}^{\rm qh}(\Omega,T) + A_{\rm ion}^{\rm ah}(\Omega,T) \ . \tag{12}$$

The former contribution has been directly calculated from MGPT quasiharmonic phonon frequencies $\nu_\lambda(\mathbf{q},\Omega)$ of the A15 crystal structure using the standard expression

$$A_{\rm ion}^{\rm qh}(\Omega,T) = \frac{k_{\rm B}T}{N}\sum_{\mathbf{q},\lambda} \ln\{2\sinh[h\nu_\lambda(\mathbf{q},\Omega)/(2k_{\rm B}T)]\} \ , \tag{13}$$

where the sum is over all wave vectors $\mathbf{q}$ and phonon branches λ in the first Brillouin zone (BZ) of the simple-cubic reciprocal lattice. With 8 atoms per primitive cell in the A15 structure, there are 24 phonon branches at each $\mathbf{q}$ point, and we find that the sum in

Eq. (13) is well converged at all volumes and temperatures with only 56 **q** points in the irreducible (1/48th) wedge of the simple-cubic BZ. In this manner, $A_{\rm ion}^{\rm qh}(\Omega,T)$ for the A15 structure has been evaluated as a function of volume and temperature over the full 29-volume mesh defined in Ref. [14], which ranges between $x=1.08$ and $x=0.80$, where $x\equiv(\Omega/\Omega_0)^{1/3}$.

The corresponding anharmonic contribution to the A15 ion-thermal free energy has been calculated from the following RSMD expression derived in Ref. [14]:

$$A_{\rm ion}^{\rm ah}(\Omega,T)=\frac{T}{T_{\rm ref}}[E_0(\Omega)+W_{\rm ion}(\Omega,T)]+\frac{3}{2}k_{\rm B}T\ln\frac{T}{T_{\rm ref}}-E_0(\Omega)\ , \tag{14}$$

where $W_{\rm ion}(\Omega,T)$ is obtained from single MGPT-RSMD simulations along selected isochores via Eq. (13) of Ref. [14]. Here, as done for the bcc structure in Ref. [14], each simulation has been started from a chosen volume-dependent reference temperature $T_{\rm ref}=0.8\Theta_D(\Omega)$ and carried though the estimated melt temperature at that volume. For the A15 structure, the RSMD simulations of $W_{\rm ion}(\Omega,T)$ have been performed in small cells of 216 atoms along eight isochores spaced in intervals of $\Delta x=0.04$. Also as done for the bcc structure in Ref. [14], each simulated isochore has been smoothly fit with a five-term polynomial of the form

$$A_{\rm ion}^{\rm ah}(\Omega,T)=A_2T^2+A_3T^3+A_4T^4+A_5T^5+A_6T^6\ , \tag{15}$$

where the A_n are volume-dependent coefficients. The smooth values of $A_{\rm ion}^{\rm ah}$ so obtained have then been extended to the full 29-volume mesh by numerical interpolation. The A15 values of $A_{\rm ion}^{\rm ah}$ so calculated are generally small, but larger than those of bcc, ranging in magnitude from 5–12 mRy near melt, as compared with only 1–5 mRy for bcc.

Total free energies for the A15 structure have been assembled both with and without the small additional electron-thermal component $A_{\rm el}$, and then combined with the liquid free energy calculated in Ref. [14] to obtain free-energy-based A15 melt curves. As shown in

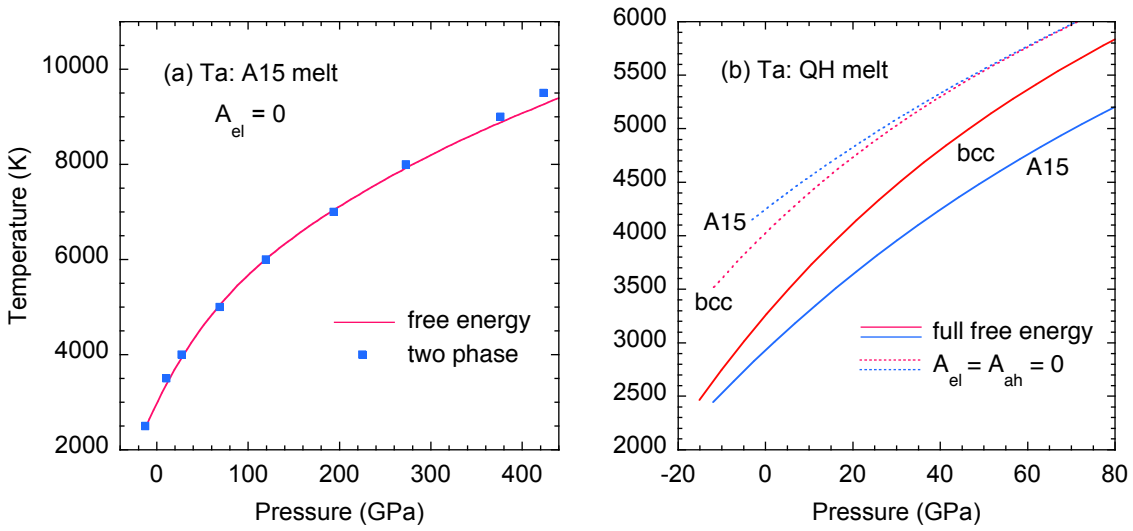

FIG. 19. Predicted aspects of MGPT A15 melting. (a) Free-energy vs. two-phase melt curve in the $A_{\rm el}=0$ limit; (b) Low-pressure A15 vs bcc melt curves obtained with full free energies and in the quasiharmonic (QH) limit with $A_{\rm el}=A_{\rm ah}\equiv A_{\rm ion}^{\rm ah}=0$.

Fig. 19(a) in the $A_{\rm el}=0$ limit, the free-energy A15 melt curve is in good agreement with that obtained in Paper I from direct two-phase simulation. As expected, the impact of $A_{\rm el}$ on A15 melting is small, lowering the melt temperatures by 3% or less, as previously found for the bcc and fcc structures [14,32]. Full free-energy melt curves for bcc and A15 are compared at pressures below 80 GPa in Fig. 19(b). In agreement with experimental observation [44], A15 is predicted to be metastable, with a melt curve close to but everywhere below that of bcc. Interestingly, however, and as also shown in Fig. 19(b), removing the anharmonic component $A_{\rm ion}^{\rm ah}$ from the solid free energy in each case significantly raises the bcc and A15 melt temperatures and reverses the ordering of the melt curves at low pressure. That is, in the quasiharmonic limit with $A_{\rm el}=A_{\rm ion}^{\rm ah}=0$, we predict A15 to be the melting phase of Ta below 40 GPa. This shows the importance of even small anharmonic effects to the high-temperature phase diagram.

One further point should also be mentioned in connection with Fig. 19(a). Although the two-phase melt curve used for comparison with the free-energy result in that figure is for the large 39,304 solid subcell considered in Paper I, this has been done for convenience

only. Because A15 is only weakly anharmonic, we have subsequently been able to verify that the A15 two-phase melt curve is already converged with a much smaller 512-atom solid subcell, which is then more consistent with the 216-atom solid subcell used in the anharmonic free-energy calculation.

B. *Pnma* and *Fddd* with $T = T_{\mathrm{m}}$ reference

For the *Pnma* and *Fddd* structures, the large-cell two-phase melt calculations discussed in Sec. IV(d) can be combined with the previously determined free energy of the liquid from Ref. [14] to establish a reference free energy along the solidus melt line in the $A_{\mathrm{el}} = 0$ limit. From the two-phase melt calculations for each structure, we have first extracted and fit the melt temperature T_{m} and pressure P_{m} as a function of the solidus volume Ω_{sol} in the general forms

$$T_{\mathrm{m}}(x) = t_0 + t_1 x + t_2 x^2 + t_3 x^3 \tag{16}$$

and

$$P_{\mathrm{m}}(x) = p_0 + p_1 x + p_2 x^2 + p_3 x^3 , \tag{17}$$

where the t_n and p_n are the fitting constants and where $x = (\Omega_{\mathrm{sol}} / \Omega_0)^{1/3}$ within the restricted volume range $1.04 \le x \le 0.80$.

Along the melt line, the melt temperature T_{m}, melt pressure P_{m}, and Gibbs free energy, $G = A + P\Omega$, of the liquid and the solid must be equal, so the Helmholtz free energy of the orthorhombic solid along the solidus melt line can be calculated as

$$A_{\mathrm{sol}}(\Omega_{\mathrm{sol}}, T_{\mathrm{m}}) = A_{\mathrm{liq}}(\Omega_{\mathrm{liq}}, T_{\mathrm{m}}) + P_{\mathrm{m}}(\Omega_{\mathrm{liq}} - \Omega_{\mathrm{sol}}) \ . \tag{18}$$

For given values of T_{m}, P_{m}, and the solidus volume Ω_{sol} on the melt curve, the corresponding liquidus volume Ω_{liq} and free energy $A_{\mathrm{liq}}(\Omega_{\mathrm{liq}}, T_{\mathrm{m}})$ can be obtained via interpolation on the liquid equation of state (calculated in the $A_{\mathrm{el}} = 0$ limit). With

$T_{\rm ref} = T_{\rm m}$ and $\Omega = \Omega_{\rm sol}$, Eq. (18) can be used directly to establish the reference free energy for the orthorhombic solid,

$$A_{\rm ion}^{\rm sol}(\Omega, T_{\rm ref}) = A_{\rm ion}^{\rm sol}(\Omega, T_{\rm m}) = A_{\rm sol}(\Omega_{\rm sol}, T_{\rm m}) - E_0(\Omega_{\rm sol}) \ , \tag{19}$$

that is needed in the RSMD simulations. In this regard, the above RMSD expression (14) is replaced by

$$A_{\rm ion}^{\rm sol}(\Omega, T) = \frac{T}{T_{\rm m}}[E_0(\Omega) + A_{\rm ion}^{\rm sol}(\Omega, T_{\rm m}) + W_{\rm ion}(\Omega, T)] - \frac{3}{2}k_{\rm B}T \ln\frac{T}{T_{\rm m}} - E_0(\Omega) \ . \tag{20}$$

One can then simulate $W_{\rm ion}(\Omega, T)$ and apply Eq. (20) both upward in temperature from $T = T_{\rm m}$ to the desired maximum $T = T_{\rm max}$ and downward in temperature from $T = T_{\rm m}$ to an allowable minimum $T = T_{\rm min}$. Once $A_{\rm ion}^{\rm sol}(\Omega, T)$ is thereby calculated for the volumes and temperatures of interest, the electron-thermal component $A_{\rm el}(\Omega, T)$ can finally be added to it to establish a total free energy and equation of state for the orthorhombic phase in question.

For the *Pnma* and *Fddd* structures, we have performed MGPT-RSMD simulations to higher and lower temperature along seven isochores contained within the restricted volume range of Eqs. (16) and (17), in increments of $\Delta x = 0.04$. The simulations to higher temperature were carried out in each case from $T_{\rm m}$ to $T_{\rm max} = 17{,}500$ K, while those to lower temperature were performed from $T_{\rm m}$ to $\sim 0.5T_{\rm m}$. The ion-thermal free-energy data so obtained for the *Pnma* and *Fddd* solids were then fit respectively with an analytic form analogous to Eq. (48) of Ref. [14] for the liquid:

$$\begin{aligned} A_{\rm ion}^{\rm sol}(\Omega, T) = {} & B_0\tau - B_1\tau\ln\tau + B_2\tau(\tau - 1) + B_3\tau(\tau^2 - 1) + B_4\tau(\tau^3 - 1) \\ & + B_5\tau(\tau^4 - 1) + B_6\tau(\tau^5 - 1) \end{aligned} \ , \tag{21}$$

where $\tau = T / T_{\rm max}$, the B_n are volume-dependent coefficients, and $B_0(\Omega) = A_{\rm ion}^{\rm sol}(\Omega, T_{\rm max})$. The values of $A_{\rm ion}^{\rm sol}$ so calculated were then extended to a fine 25-volume mesh with $\Delta x = 0.01$ by numerical interpolation.

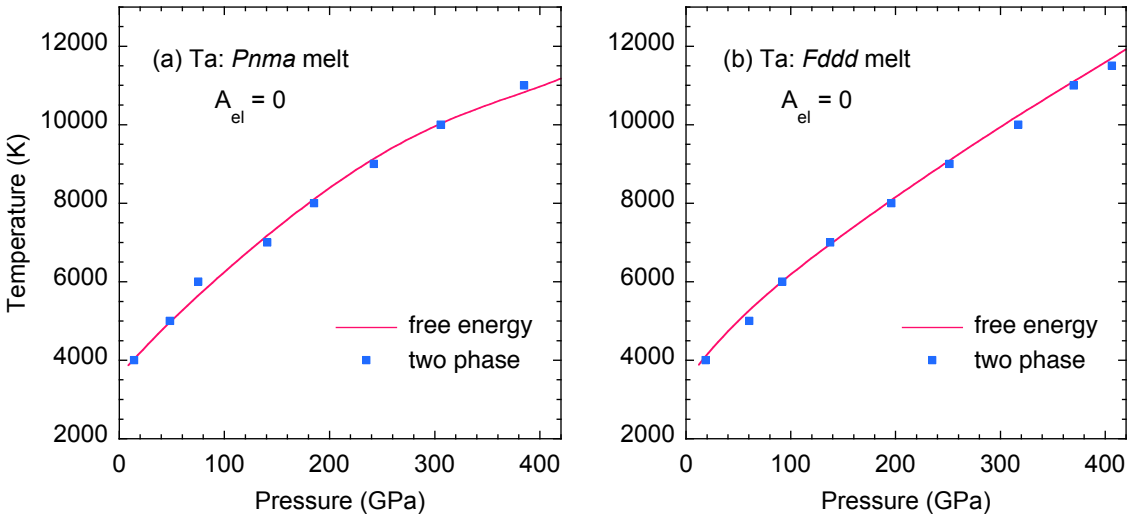

FIG. 20. Calculated MGPT orthorhombic free-energy melt curves in Ta compared with corresponding input two-phase melt data in the $A_{\rm el}=0$ limit. (a) *Pnma* ; (b) *Fddd*.

To test the numerical accuracy and self-consistency of our calculations of $A_{\rm ion}^{\rm sol}(\Omega,T)$ for *Pnma* and *Fddd*, the total free energy in the $A_{\rm el}=0$ limit for each solid was obtained by adding the appropriate cold energy $E_0(\Omega)$. These results were then used together with the established liquid free energy to perform Helmholtz free-energy calculations of the *Pnma* and *Fddd* melt curves. The $A_{\rm el}=0$ free-energy melt curves so calculated are compared with the input two-phase melt data in Fig. 20. The agreement is seen to be generally good for both *Pnma* and *Fddd*. As a final step, we have added the electron-thermal contribution $A_{\rm el}(\Omega,T)$ to form total *Pnma* and *Fddd* free energies at the same level of approximation as obtained for the bcc, fcc and A15 structures. As expected, the impact of $A_{\rm el}$ on the *Pnma* and *Fddd* melt curves was found to be small, lowering the calculated melt temperatures by 3% or less at all pressures, as was also the case for bcc, fcc and A15.

VI. SUMMARY and CONCLUSIONS

In this paper we have extended the quantum-based MGPT studies begun in Paper I of possible high-T,P polymorphism in the phase diagram of Ta to include four promising orthorhombic structures: *Pnma*, *Fddd*, *Pmma* and *Cmcm* or α-U, in addition to the cubic bcc, fcc and A15 structures and the hexagonal hcp and ω structures treated in Paper I. Thus, including the liquid, a total of ten phases have been studied. For the nine solid phases treated, both low- and high-temperature mechanical and thermodynamic stability have been addressed in detail at high pressures up to 420 GPa. A summary of some the main results obtained here and in Paper I is given in Table I.

In the low-T solid, mechanical stability has been determined on the basis of calculated $T = 0$ quasiharmonic phonons, with the bcc, A15, *Pnma* and *Fddd* structures predicted to be stable from ambient conditions to 420 GPa in pressure, with similar pressure-dependent Debye temperatures calculated for all four phases. The fcc, hcp, hex-ω, *Pmma* and α-U structures were found to be mechanically unstable at all volumes over the same pressure range. Corresponding structural and thermodynamic stability has been determined by relaxed $T = 0$ total-energy calculations, with bcc producing the lowest total energy at all pressures, and with A15, *Fddd* and *Pnma*, respectively, being the structures next lowest in total energy. Upon heating in constant-volume MGPT-MD simulations, the *Fddd* and *Pnma* structures were found to undergo temperature-induced phase transitions to bcc at all volumes, with transition temperatures in the range 150-1450 K. The transition temperatures attain peak values for these structures in the pressure range 80-150 GPa.

In the high-T solid, accurate results on the mechanical and thermodynamic stability have been determined on the basis of large-cell MGPT-MD simulations. Large anharmonic effects have been found over the pressure range 0-420 GPa in all structures, with the exception of bcc and A15. In the cases of fcc, hcp, hex-ω, *Pmma* and α-U, this large anharmonicity is the principle driving force that mechanically stabilizes these structures at high temperature. For hex-ω, however, high-T mechanical stability is sensitive to the

TABLE I. Summary of the MGPT predicted low- and high-temperature mechanical and thermodynamic stability of nine solid crystal structures in Ta to 420 GPa.

Solid phase	Low-T mechanical stability	Low-T thermodynamic stability	T-induced solid-solid phase transition	High-T mechanical stability	High-T thermodynamic stability
bcc	yes	yes	no	yes	yes
fcc	no	no	—	yes	no
hcp	no	no	—	yes	no
A15	yes	no	no	yes	no; metastable (~ 0-80 GPa)
hex-ω	no	no	—	$c/a < 0.54$ only	no
Pnma	yes	no	to bcc	yes	co-exist *w*. bcc (~ 90 GPa)
Fddd	yes	no	to bcc	yes	co-exist *w*. bcc (~ 90-140 GPa)
Pmma	no	no	—	yes	no
α-U	no	no	—	yes	co-exist *w*. bcc (~ 90 GPa)

c/a axial ratio and only occurs for $c/a < 0.54$. For $c/a > 0.54$, hex-ω remains mechanically unstable and partially transforms to bcc.

The large anharmonic effects found in our candidate structures at high temperature also give rise to important *melt size effects*, which can strongly impact any predictions of thermodynamic phase stability on the basis of relative melt curves. In Paper I, we found for the cubic and hexagonal phases of Ta that solid-phase MD cells needed to be at least ~ 500 atoms to produce accurate melt curves. This finding reversed the small-cell (< 150 atom) QMD prediction [12] of a thermodynamically stable hex-ω phase. Here we have shown for the orthorhombic phases that the solid-phase MD cell needs to be significantly larger and at least ~ 1000–4000 atoms to avoid melt size effects. This reverses the recent

small-cell (64 atom) DFT metadynamics [15] and (~ 500 atom) QMD [19] predictions of a thermodynamically stable *Pnma* phase.

In Paper I and the present paper, we have determined accurate high-T thermodynamic stability using large-cell two-phase MGPT-MD melt simulations with solid-phase cell sizes of ~ 40,000 atoms and total cell sizes of ~ 80,000 atoms. For the fcc, hcp, A15, hex-ω and *Pmma* structures, our calculated melt curves all clearly lie below that of bcc, supporting bcc thermodynamic stability. In the case of A15, the calculated melt curve begins to closely approach the bcc melt curve below 80 GPa, consistent with the observed metastability of the A15 phase at ambient pressure [44]. For the remaining *Fddd*, *Pnma* and α-U structures, our two-phase melt curves all touch (but do not cross above) the bcc melt curve in the vicinity of 100 GPa, suggesting that these phases could co-exist with bcc in this vicinity, and possibly be observed experimentally.

Finally, we have here calculated MGPT global free energies for the A15, *Pnma* and *Fddd* phases of Ta to complement those determined for the bcc, fcc and liquid phases in Ref. [14]. Free-energy based melt curves calculated for the bcc, fcc, A15, *Pnma* and *Fddd* structures are all consistent with our large-cell, two-phase results. In addition, analysis of the A15 free-energy components show directly that it is the small, but larger than bcc, anharmonic free energy in A15 that prevents this structure from becoming the thermodynamically stable phase at low pressure. In the quasiharmonic limit, without anharmonic effects, A15 is predicted to be the stable high-T phase of Ta below about 40 GPa.

ACKNOWLEDGMENTS

The work of J.A.M. was performed under the auspices of the U.S. Department of Energy by Lawrence Livermore National Laboratory under Contract No. DE-AC52-07NA27344. The authors wish to thank Tom Lenosky for pointing out the competitive nature of the *Pmma* structure with bcc found for Mo in Ref. [42].

REFERENCES

[1] D. Errandonea, B. Schwager, R. Ditz, C Gessmann, R. Boehler, and M. Ross, Phys. Rev. B **63**, 132104 (2001).

[2] D. Errandonea, M. Somayazulu, D. Häusermann, and H. K. Mao, J. Phys.: Condens. Matter **15**, 7635 (2003).

[3] D. Santamría-Perez, M. Ross, D. Errandonea, G. D. Mukherjee, M. Mezouar, and R. Boehler, J. Chem. Phys. **130**, 124509 (2009).

[4] J. W. Shaner, G. R. Gathers, and W. M. Hodgson, in *Proceedings of the Seventh Symposium on Thermophysical Properties*, edited by A. Cezairliyan, (ASME, New York, 1977), pp. 896-903.

[5] J. W. Shaner, G. R. Gathers, and C. Minichino, High Temp. High Pressures **9**, 331 (1977).

[6] A. Berthault, L. Arles, and J. Matricon, International J. Thermophysics **7**, 167 (1986).

[7] R. S. Hixson and M. A. Winkler, International J. Thermophysics **11**, 709 (1990).

[8] J. M. Brown and J. W. Shaner, in *Shock Waves in Condensed Matter – 1983*, edited by J. R. Asay, R. A. Graham, and G. K. Straub, (Elsevier, Amsterdam, 1984), pp. 91-94.

[9] R. S. Hixson, D. A. Boness, J. W. Shaner, and J. A. Moriarty, Phys. Rev. Lett. **62**, 637 (1989).

[10] C. Dai, X. Jin, X. Zhou, J. Liu, and J. Hu, J. Phys. D: Appl. Phys. **34**, 3064 (2001).

[11] C. Dai, J. Hu, and H. Tan, J. Appl. Phys. **106**, 043519 (2009).

[12] L. Burakovsky, S. P. Chen, D. L. Preston, A. B. Belonoshko, A. Rosengren, A. S. Mikhaylushkin, S. I. Simak, and J. A. Moriarty, Phys. Rev. Lett. **104**, 255702 (2010).

[13] J. B. Haskins, J. A. Moriarty, and R. Q. Hood, Phys. Rev. B **86**, 224104 (2012). Referred to in the text as Paper I.

[14] J. A. Moriarty and J. B. Haskins, Phys. Rev. B **90**, 054113 (2014).

[15] Y. Yao and D. D. Klug, Phys. Rev. B **88**, 054102 (2013).

[16] Z.-L. Liu, L.-C. Cai, X.-L. Zhang, and F. Xi, J. Appl. Phys. **114**, 073520 (2013).

[17] L. L. Hsiung, J. Phys.: Condens. Matter **22**, 385702 (2010).

[18] C.-H. Lu, E. N. Hahn, B. A. Remington, B. R. Maddox, E. M. Bringa, and M. A. Meyers, Sci. Rep. **5**, 15064 (2015).

[19] L. Burakovsky, S. P. Chen, D. L. Preston, and D. G. Sheppard, J. Phys.: Conf. Series **500**, 162001 (2014).

[20] A. Dewaele, M. Mezouar, N. Guignot, and P. Loubeyre, Phys. Rev Lett. **104**, 255701 (2010).

[21] A. Karandikar and R. Boehler, Phys. Rev. B **93**, 054107 (2016).

[22] W. Kohn and L. J. Sham, Phys. Rev. **140**, A1133 (1965); N. D. Mermin, Phys. Rev. **137**, A1441 (1965).

[23] A. B. Belonoshko, N. V. Skorodumova, A. Rosengren, and B. Johansson, Phys. Rev. B **73**, 012201 (2006); A. B. Belonoshko, L. Burakovsky, S. P. Chen, B. Johansson, A. S. Mikhaylushkin, D. L. Preston, S. I. Simak, and D. C. Swift, Phys. Rev. Lett. **100**, 135701 (2008).

[24] L. L. Hsiung and D. H. Lassila, Scr. Mater. **38**, 1371 (1998); **39**, 603 (1998); Acta Mater. **48**, 4851 (2000).

[25] S. Taioli, C. Cazorla, M. J. Gillan, and D. Alfè, Phys. Rev. B **75**, 214103 (2007).

[26] J. A. Moriarty Phys. Rev. B **38**, 3199 (1988).

[27] J. A. Moriarty, Phys. Rev. B **42**, 1609 (1990); **49**, 12431 (1994).

[28] J. A. Moriarty, L. X. Benedict, J. N. Glosli, R. Q. Hood, D. A. Orlikowski, M. V. Patel, P. Söderlind, F. H. Streitz, M. Tang, and L. H. Yang, J. Mater. Res. **21**, 563 (2006).

[29] F. H. Streitz, J. N. Glosli, M. V. Patel, B. Chan, R. K. Yates, B. R. de Supinski, J. Sexton, and J. A. Gunnels, J. Phys.: Conf. Series **46**, 254 (2006).

[30] S. Plimton, J. Comput. Phys. 117, 1 (1995). The web site for the LAMMPS code is http://lammps.sandia.gov

[31] J. A. Moriarty, R. Q. Hood, and L. H. Yang, Phys. Rev. Lett. **108**, 036401 (2012).

[32] J. A. Moriarty, J. F. Belak, R. E. Rudd, P. Söderlind, F. H. Streitz, and L. H. Yang, J. Phys.: Condens. Matter **14**, 2825 (2002).

[33] J. R. Morris, C. Z. Wang, K. M. Ho, and C. T. Chan, Phys. Rev. B **49**, 3109 (1994).

[34] E. R. Hernández, A. Rodriguez-Prieto, A. Bergara, and D. Alfè, Phys. Rev. Lett. **104**, 185701 (2010).

[35] R. Q. Hood, L. H. Yang, and J. A. Moriarty, Phys. Rev. B **78**, 024116 (2008).

[36] R. Q. Hood (unpublished, 2010).

[37] L. G. Wang, A. van de Walle, and D. Alfè, Phys. Rev. B **84**, 092102 (2011).

[38] M. Pozzo and D. Alfè, Phys. Rev. B **88**, 024111 (2013).

[39] D. A. Young, Phase Diagrams of the Elements (University of California, Berkeley, 1991).

[40] S. Heathman, R. G. Haire, T. Le Bihan, A. Lindbaum, K. Litfin, Y. Méresse, and H. Libotte, Phys. Rev. Lett. **85**, 2961 (2000).

[41] Y. Nakamoto, M. Sakata, K. Shimizu, H. Fujihisa, T. Matsuoka, Y. Ohishi, and T. Kikegawa, Phys. Rev. B **81**, 140106 (2010).

[42] H. Park, M. R. Fellinger, T. J. Lenosky, W. W. Tipton, D. R. Trinkle, S. P. Rudin, C. Woodward, J. W. Wilkins, and R. G. Hennig, Phys. Rev. B **85**, 214121 (2012).

[43] P. Söderlind and J. A. Moriarty, Phys. Rev. B **57**, 10340 (1998).

[44] L. Cortella, B. Vinet, P. J. Desre, A. Pasturel, A. T. Paxton, and M. van Schilfgaarde, Phys. Rev. Lett. **70**, 1469 (1993).